

Observation of the quantum equivalence principle for matter-waves

Or Dobkowski,¹ Barak Trok,¹ Peter Skakunenko,¹ Yonathan Japha,¹ David Groswasser,¹ Maxim Efremov,^{2,3} Chiara Marletto,⁴ Ivette Fuentes,^{5,6} Roger Penrose,⁷ Vlatko Vedral,⁴ Wolfgang P. Schleich,^{3,8} and Ron Folman¹

¹*Ben-Gurion University of the Negev, Department of Physics and Ilse Katz Institute for Nanoscale Science and Technology, Be'er Sheva 84105, Israel*

²*German Aerospace Center (DLR), Institute of Quantum Technologies, 89081 Ulm, Germany*

³*Institut für Quantenphysik and Center for Integrated Quantum Science and Technology (IQST), Universität Ulm, 89081 Ulm, Germany*

⁴*Clarendon Laboratory, University of Oxford, Parks Road, Oxford OX1 3PU, United Kingdom*

⁵*School of Physics and Astronomy, University of Southampton, Southampton SO17 1BJ, United Kingdom*

⁶*Keble College, University of Oxford, Oxford OX1 3PG, United Kingdom*

⁷*Mathematical Institute, Andrew Wiles Building, University of Oxford, Radcliffe Observatory Quarter, Woodstock Road, Oxford, OX2 6GG, United Kingdom*

⁸*Hagler Institute for Advanced Study at Texas A&M University, Texas A&M AgriLife Research, Institute for Quantum Science and Engineering (IQSE), and Department of Physics and Astronomy, Texas A&M University, College Station, Texas 77843-4242, USA*

Einstein's general theory of relativity is based on the principle of equivalence — in essence, dating back to Galileo — which asserts that, locally, the effect of a gravitational field is equivalent to that of an accelerating reference frame, so that the local gravitational field is eliminated in a freely falling frame. Einstein's theory enables this principle to extend to a global description of relativistic space-time, at the expense of allowing space-time to become curved, realising a consistent frame-independent description of nature at the classical level. Einstein's theory has been confirmed to great accuracy for astrophysical bodies. However, in the quantum domain the equivalence principle has been predicted to take a unique form involving a gauge phase that is observable if the wavefunction — fundamental to quantum descriptions — allows an object to interfere with itself after being simultaneously at rest in two differently accelerating frames, one being the laboratory (Newtonian) frame and the other in the freely-falling (Einsteinian) frame. To measure this gauge phase we realise a novel cold-atom interferometer in which one wave packet stays static in the laboratory frame while the other is in free-fall. We follow the relative-phase evolution of the wave packets in the two frames, confirming the equivalence principle in the quantum domain. Our observation is yet another fundamental test of the interface between quantum theory and gravity. The new interferometer also opens the door for further probing of the latter interface, as well as to searches for new physics.

I. INTRODUCTION

Ever since Galileo and Newton, it was clear that the phenomenon of free-fall in a gravitational field is a paradigm of physics, and must be fully understood as part of any description of nature. Einstein went a step further and used the geometry of space-time to describe gravity and free-fall. In addition, an assertion of paramount importance in physics is that to be consistent one should be able to describe nature from different frames of reference, where once more the freely-falling frame is considered fundamental. This led to the formulation of the equivalence principle, which again deals with gravity [1–3]. The rise of quantum mechanics has not changed any of these convictions, and it remains to be seen how quantum theory adheres to them. The connection between gravity (or general relativity) and quantum theory, the two pillars of modern physics, remains one of the most important open questions in physics.

Here we present a direct observation of the quantum phase of a free-falling object, confirming the quantum equivalence principle for matter-waves. Measuring gravity with quantum interferometers has been previously achieved with neutrons in the celebrated Colella-Overhauser-Werner (COW) experiment [4] (as well as by Bonse and Wroblewski for a noninertial frame [5]), and with atoms [6–10], but the explicit phase of a free-falling wave packet has not been directly measured. This requires a unique interferometer in which one trajectory is stationary in the lab frame (relative to Earth) and acts as a reference, while the other is in free fall.

We use in the following the common definition of the equivalence principle, as Einstein originally thought of it: A state of rest in a homogeneous gravitational field is physically indistinguishable from a

state of uniform acceleration in a gravity-free space [11]. Let us note that numerous possible extensions of the equivalence principle to the quantum domain (hereafter the “quantum equivalence principle”) have been proposed [12–19] and here we focus on the most straightforward aspect, which is the quantum phase connecting between the freely-falling frame and the lab frame [20], termed by some the Einsteinian and Newtonian frames, respectively [21]. This phase has a characteristic dependence of t^3 on the free-fall time t [3, 20, 21]. As this phase dependence is based on the assumption that the inertial mass is equal to the gravitational mass, as suggested by Galileo and as confirmed experimentally with early experiments by Newton, Bessel and Eötvös and more recent experiments with improved accuracy [22–24], we name our unique interferometer the Quantum Galileo Interferometer, or QGI [25].

The prediction that an accelerated object, and specifically a free-falling object acquires a t^3 -phase, has been made quite some time ago by Darwin, Kennard and others [26–34]. While a cubic phase dependence on the interferometer time may also appear in a few standard-practice interferometers [35–39], observing this free-fall phase in the QGI configuration sampling these two fundamental frames, constitutes a direct test and confirmation of the phase of a free-falling object, as well as a fundamental aspect of the quantum equivalence principle for matter waves [3, 17, 20].

The transformation between the wavefunction ψ_N in a Newtonian (laboratory) frame of reference, where the acceleration of an object is due to gravity, $\ddot{z} = -g$, and the wavefunction ψ_E in an Einsteinian frame that falls in gravity together with free-falling objects, and when at $t = 0$ both have the same velocity, involves a phase (e.g., Eq. 5 in Ref. [21]) which may also be referred to as a gauge phase ϕ_{gauge} [20] [see supplementary material (SM)]

$$\psi_N(z, t) = e^{i\phi_{\text{gauge}}(z, t)} \psi_E(z + g \frac{t^2}{2}, t), \text{ where } \phi_{\text{gauge}} = \frac{m}{\hbar} \left(-\frac{1}{6} g^2 t^3 - g z t \right). \quad (1)$$

This fundamental phase plays two roles: first, it is the phase difference between the same wave packet as viewed from the Einsteinian and Newtonian frames in a gravitational field (e.g., Eq. 5 in Ref. [21]); second, as explained in Ref. [20], it is the phase between a wave packet in a frame accelerated with acceleration $a = -g$ in an environment devoid of gravity, and an identical wave packet in a frame that is at rest in a gravitational field, such that the two systems are indistinguishable as the phase cannot be measured by any local operation – thus heralding the quantum equivalence principle.

Our experiment intended to measure this fundamental phase — by way of interference with a reference wave packet — follows a *Gedanken* (thought) experiment where at time $t = t_0$ the wave packet is split into two paths where in one path it is at rest in the Newtonian frame, due to an applied force that is exactly opposite to gravity, while in the other path it is in free-fall, namely, at rest in the freely-falling Einsteinian frame. To achieve recombination of the two paths, the wave packet in the freely falling path is initially launched upwards by a magnetic-gradient pulse with a velocity v_0 in the direction opposite to gravity and then falls freely for a time $2T = 2v_0/g$ (hereafter referred to as the closing condition), after which an identical magnetic-gradient pulse erases the velocity difference between the two wave packets so that the two paths overlap in position and momentum. Fig. 1(A) describes this *Gedanken* experiment, where the wave packet that is at rest in the lab (Newtonian) frame is termed the “reference wave packet” while the wave packet that is free-falling in the lab (Newtonian) frame is termed the “ballistic wave packet” [40].

For an intuitive understanding of the QGI in the Newtonian frame, we fix the reference wave packet center at vertical position $z = 0$ so that it does not accumulate any propagation phase (beyond the free evolution of the wave packet), and calculate the phase accumulated by the ballistic wave packet. The latter accumulates no propagation phase in the freely-falling (Einsteinian) frame, and we can use the gauge phase to know its phase in the Newtonian frame. We calculate the phase in the ballistic path in two parts: First, a wave packet starting at $t = 0$ in the middle of the interferometer and going forward in time, and then starting from the same point and going backward in time, with these paths ending at $t = \pm T$ and $z = 0$ after a free-fall duration of T [Fig. 1(A)]. It follows that the gauge phase at the center of the wave packet for the two parts, and the phase difference between the two end points read

$$\phi_{\text{gauge}}(\pm T) = \mp \frac{m}{6\hbar} g^2 T^3; \phi_{\text{ballistic}} = \phi_{\text{gauge}}(T) - \phi_{\text{gauge}}(-T) = -2 \cdot \frac{m}{6\hbar} g^2 T^3, \quad (2)$$

where the linear phase contribution in Eq. (1) is canceled by the magnetic-gradient pulses (SM). In the SM we arrive at the same result also by starting from the Galilean transformation. Consequently, $\phi_{\text{ballistic}}$ is the relative phase observable in the experiment.

In fact, the QGI also demonstrates a quantum equivalence principle between the Newtonian and Einsteinian frames, for a quantum system in a state of spatial superposition. This is due to the complete

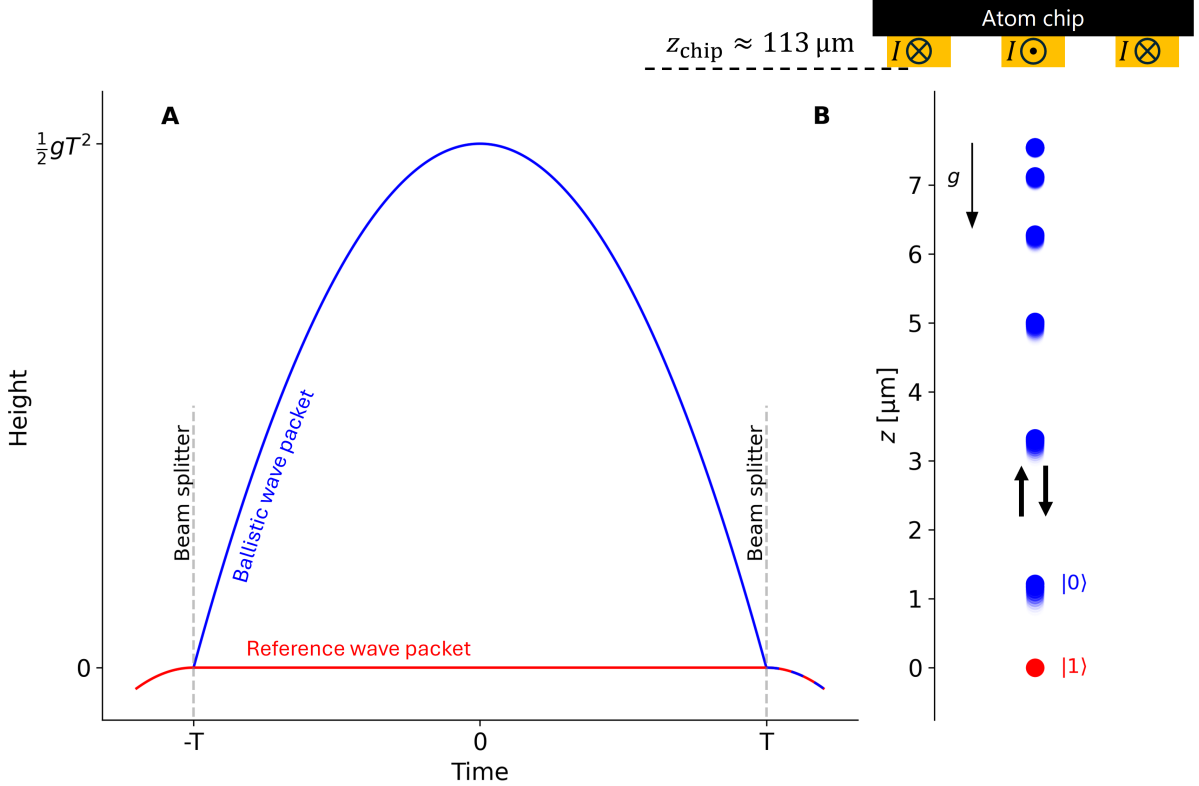


FIG. 1: The QGI experiment to measure the phase accumulation of a free-falling particle. (A) Space-time diagram illustrating the classical trajectories of the wave packets in the interferometer. A beam splitter creates a coherent superposition of two wave packets with different spin states, launching one wave packet into a freely-falling ballistic trajectory for a duration of $2T$, while the second wave packet is held stationary, serving as a reference. A second beam splitter recombines the two wave packets at the end of the ballistic trajectory. State-dependent detection (not shown) measures the population in each state, revealing the phase difference between the two trajectories. (B) A schematic of our experimental realization: The stationary trajectory is held against gravity using magnetic gradients produced by currents in microfabricated wires on the atom chip. The stationary trajectory, associated with state $|1\rangle \equiv |F = 2, m_F = 1\rangle$ of a ^{87}Rb atom, is positioned $\approx 113\text{ }\mu\text{m}$ below the chip surface. The ballistic trajectory, associated with state $|0\rangle \equiv |F = 1, m_F = 0\rangle$, travels upwards reaching, in this example, a splitting of about $7.5\text{ }\mu\text{m}$ [about seven times the wave packet size (SM)]. The interchanging currents in the three wires (shown in the figure) create a 2D quadrupole to realize a strong magnetic gradient with a small magnetic field, which minimizes phase noise. See the Methods section for more details.

symmetry of the QGI. An observer sitting in the Einsteinian or Newtonian frames will see exactly the same phenomenon, with the roles of the reference wave packet and the ballistic wave packet inverted. This symmetry becomes strikingly clear when one computes the actions in both frames (SM). Assuming that the inertial and gravitational masses are equal and that the acceleration we induce by an external force to form the reference trajectory is exactly opposite to the gravitational acceleration, the action of the ballistic path in the Newtonian frame and that of the reference path in the Einsteinian frame are the same, equal to $-\frac{m}{3}g^2T^3$ [41].

Finally, the QGI is able to measure the quantum equivalence principle for matter waves, as it utilizes no electromagnetic waves resonant with some atomic transition. In contrast, in interferometers based on light pulses, one must take into account the electromagnetic fields, namely, introduce transformations of Maxwell equations, so that a working interferometer may be described in both frames. Consequently, in such interferometers, what is in fact verified is the equivalence principle for electromagnetic waves [42, 43] (see SM). In the QGI, no such additional theoretical structure needs to be invoked.

To conclude, it may then be understood that the QGI is able to fully test the quantum equivalence principle for matter waves due to two main reasons: First, it is a configuration in which one wave packet is

at rest in an inertial frame while the other is at rest in a freely-falling frame, and second, by only utilizing the theory of de-Broglie waves it achieves the complete symmetry required for testing the equivalence principle for matter waves.

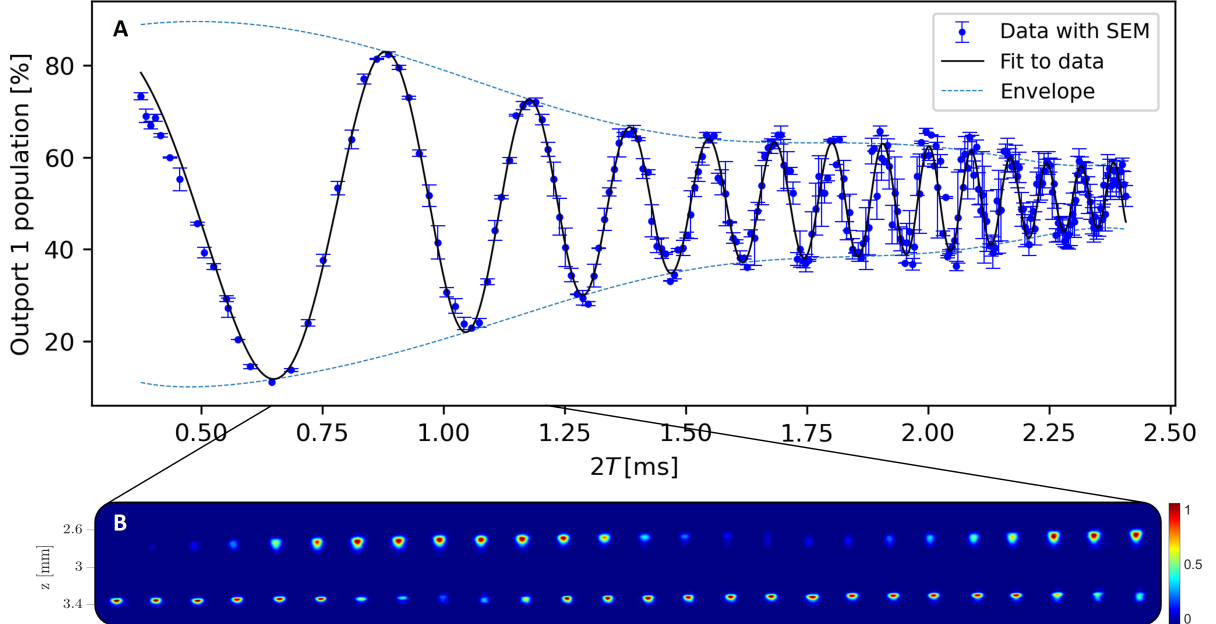


FIG. 2: Population in outport 1 vs. the free-fall duration of the ballistic path $2T$.
 (A) The relative spin population in outport 1 (state $|0\rangle$) oscillates with a distinct chirp as a function of interferometer time. The blue points represent the experimental data, with error bars derived from the standard error of the mean (SEM). The black line is a fit to the data of the form $P = P_{\text{mean}}(2T) + \frac{1}{2}V(2T) \cos[\phi(2T)]$, where V is the visibility of the oscillations, ϕ is the phase of the oscillations and P_{mean} is the mean value of the population. To obtain the fit, we first identify the upper and lower envelopes and fit them to a polynomial to get P_{mean} and $V(2T)$. We then fit the data to the model where the phase $\phi(2T)$ is a third-order polynomial. During the fitting we exclude the first and last oscillation as they suffer from larger uncertainty in the values of the envelope. The data shows 13 complete oscillations, with low phase noise, resulting in an average population error (SEM) of 1.8 ± 1.5 [%] and good visibility, starting at $V = 80\%$ and decreasing to $V = 20\%$ at $2T = 2000\mu\text{s}$. The decrease in visibility is mainly due to a varying overlap between the wave packets due to differences in shape evolution under the influence of curved gradients as well as imperfection in the path recombination. The figure includes 633 experimental cycles, each 30 s, so the graph was taken over a period of 5.3 hours. The short-term and long-term stability of the interferometer are good due to the high stability of the chip trap, and current source. (B) CCD images of the atoms in the two outports taken with on-resonance absorption imaging, showing one and a half oscillations. The top cloud is outport 1 (state $|0\rangle$), and the bottom cloud is outport 2 (state $|1\rangle$, which is magnetically sensitive), Z represents the distance from the chip, and the heatmap shows the relative optical density. The cloud in outport 2 is focused by the final splitting pulse, increasing its optical density, and making it appear slightly brighter even when the two clouds have the same population.

II. EXPERIMENT

Typical atom interferometers are free-space interferometers, whereby during most of their motion, the wave packets do not experience any potential applied by the experimental setup [44]. Some interferometers do have a potential applied to the wave packets during their evolution, and these may be termed, guided interferometers [45, 46]. In our case, both methods are used simultaneously, one for each of the wave packets.

In Fig. 1(B) we present the experimental setting in which the QGI, utilizing ^{87}Rb atoms, is conducted

about $113\ \mu\text{m}$ below an atom chip [47], where the current-carrying wires give rise to the magnetic field gradients which are responsible for the Stern-Gerlach (SG) type forces applied to the wave packets. The QGI is a novel type of SG interferometer (SGI), leveraging a decade of SGI experiments in which the necessary techniques were developed [48], and consequently, is now capable of demonstrating enhanced stability, larger phase accumulation, and especially the flexibility required to enable one wave packet to take a ballistic trajectory while the other is stationary.

During the free-fall time, the ballistic wave packet is in state $|0\rangle \equiv |F = 1, m_F = 0\rangle$, so that to first order in the Zeeman interaction it is not affected by the magnetic gradients. The reference wave packet is in state $|1\rangle \equiv |F = 2, m_F = 1\rangle$ and is held stationary by a “holding magnetic gradient pulse” producing a magnetic force counteracting gravity. Both states belong to the atomic ground state, whereby F is the total angular momentum of an atomic state and m_F is its projection on the quantization axis.

The splitting of the wave packet is not abrupt and requires a finite kick time T_{kick} in which the reference wave packet is temporarily in state $|0\rangle$ and the ballistic wave packet is temporarily in state $|1\rangle$ allowing it to be accelerated with an average acceleration $a_{\text{kick}} = v_0/T_{\text{kick}}$. In addition, a finite delay time T_d is needed between the kick pulse and the holding pulse of duration $T_h = 2T - 2T_d$, where $2T$ represents the free-fall time of the ballistic wave packet. As explained in Methods, the ballistic wave packet has a free-fall time of $2T$, while the reference wave packet is in free fall during the time $T_{\text{kick}} + T_d$ before and after the holding time. Using ϕ_{gauge} these latter parts of the reference wave packet trajectory involve a free-fall phase in the Newtonian (lab) frame of

$$\phi_{\text{reference}} = \frac{2m}{3\hbar} g^2 (T_{\text{kick}} + T_d)^3. \quad (3)$$

Consequently, the phase of the reference wave packet is independent of the holding time.

By using arguments similar to the ones used above to derive the previous equations, we can also calculate the phase of the ballistic wave packet during the kick time and obtain the total phase difference expected in the experiment (SM)

$$\Delta\phi = \frac{mg^2}{3\hbar} \left(T^3 + T^2 T_{\text{kick}} + T (T_{\text{kick}}^2 + T_{\text{kick}} T_d) - T_d (T_{\text{kick}} + T_d)^2 \right), \quad (4)$$

where the quadratic and linear dependence on the interferometer time T is due to the finite duration of the kick T_{kick} (setting $T_{\text{kick}} = 0$ eliminates them), while T_d adds a constant phase term.

Let us briefly describe in more detail the experimental sequence we have realized (more details in Methods and SM): We create a Bose-Einstein condensate (BEC) consisting of about $2 \cdot 10^4$ atoms in a magnetic trap, utilizing current-carrying wires on an atom chip (the atoms are below the chip which is upside down [Fig. 1(B)]). We then release the atom cloud from the trap and conduct a Delta-kick cooling (collimation) procedure. The atom cloud is by now dilute enough so that atom-atom interaction is minimized and the physics becomes essentially single-particle physics. After a $\pi/2$ pulse, each atom is in a superposition of a magnetic sensitive state $|1\rangle$ and a non-sensitive state $|0\rangle$.

Next, we apply a magnetic kick which launches state $|1\rangle$ upwards. Quickly thereafter, we apply a π pulse, so that the wave packet launched upwards is in state $|0\rangle$ and is no longer affected by the magnetic gradients, thus going into a ballistic trajectory affected only by gravity (up to second order Zeeman).

Conversely, the other wave packet, which is now in state $|1\rangle$, is sensitive to the magnetic gradient which is at this time tuned so that it exactly counteracts gravity. Consequently, this wave packet remains static and does not change position. Finally, we reverse the sequence to bring the two wave packets to have the same position and momentum for a full overlap.

The detection stage starts with a $\pi/2$ pulse which projects the phase difference between the spin states to the population of the states. Next, another magnetic gradient kick separates the two spin states in space, so that after some time of flight we are able to determine the population in each spin state using absorption imaging with a CCD, and thus measure the output of the interferometer.

Beyond the achievement of two very different wave packet trajectories in space, a significant experimental challenge lies in the fact that the two trajectories are very much different in momentum, and recombining the wave packets in order to observe an interference pattern requires a good overlap in both position and momentum (namely, zeroing any difference, or in other words, time-reversing the splitting process). The time-irreversibility of the splitting process, whether it be of technical or fundamental origin, has been termed by Scully, Englert and Schwinger the “Humpty-Dumpty effect” and combating it requires meticulous control over the trajectories [49].

More so, for a good overlap the size and shape of the two wave packets have to be quite similar, and as they are exposed to different magnetic gradients having different curvature, lensing effects make such

an overlap hard to achieve. Finally, also rotation of the wave packets in 3D may diminish the eventual overlap, and consequently the contrast (visibility) of the interference pattern [50].

Whereas recombination in atom interferometers based on laser pulses, even when the momentum splitting is large [51], enjoys the naturally given quantum accuracy of the photon momentum, in an SGI the momentum transfer is classical in nature. This requires a high level of control over the magnetic fields as well as a detailed simulation of the wave packet evolution when exposed to such fields and gravity [52]. The QGI indeed achieves good control over position, momentum, acceleration, as well as wave packet shape and spin.

III. RESULTS

In Fig. 2 we present the raw data, where we observe about 13 oscillations, which constitute about 80 rad phase accumulation. In Fig. 3 we analyze the phase extracted from Fig. 2, and compare it to a numerical simulation, the analytical prediction of Eq. (4) as well as to the *Gedanken* experiment [Eq. (2)]. The analytical approximation assumes square pulses of a homogeneous gradient along the z -axis giving rise to a purely one-dimensional motion along z , which together with the symmetry of the scheme results in perfect path recombination. The numerical simulation takes into account (i) three-dimensional propagation in a curved potential resulting in a non-perfect path recombination, (ii) internal wave packet dynamics (expansion, focusing and rotation) and (iii) atom-atom interactions within each wave packet. The first two factors may change the phase by an order of 1-2 radians each, while the latter may contribute up to about 0.25 radians. Obviously, the prediction of the numerical simulation is accurate to within the uncertainty limits of the experimental parameters. In the SM, we provide detailed information as to how all lines in Figs. 2 and 3 were plotted. The main source of uncertainty in the experimental results arises from the systematic uncertainty in the ratio of the kick and holding currents, as the phase accumulation is most sensitive to this ratio, where deviations from the desired ratio add a phase term that scales linearly with the interferometer time.

As can be seen from Fig. 3(B), the residuals amount to about 2.5%, presenting good agreement between the model and the data.

IV. DISCUSSION

We have realized a unique interferometer, the QGI. While the Ramsey-Bordé interferometer is mostly characterized by the constant spatial separation between the two interferometer paths [53], and the Kasevich-Chu interferometer is mostly characterized by the piece-wise constant velocity separation (difference) between the two paths [54], the QGI enables the control of all degrees of freedom, obtaining spatial, velocity and acceleration differences, almost at will. This allowed us to have one wave packet at rest and the other free-falling.

The cubic phase holds special meaning in the case of our interferometer. In this case it is equal to the phase constituting the quantum equivalence principle or the phase of the transformation between the Newtonian and Einsteinian frames of reference. Another point of view explaining how the QGI enables to probe this fundamental phase lies in the fact that it gives rise to a perfect symmetry between the two frames, as exemplified by the calculation of the actions as seen from both frames. The QGI is perfectly suited for its mission also because it does not require any transformation of electromagnetic waves, so that its physics is only a product of de-Broglie waves.

The good agreement between the data and the analytical as well as numerical prediction, brings us to conclude that we have indeed observed the phase accumulation of a free-falling object, and in doing so, we have confirmed with a high level of confidence the expected T^3 -phase behavior. We have thus observed the phase associated with the equivalence principle in the quantum domain.

As an outlook let us note two important points: First, as our unique interferometer is also able to manipulate clock wave packets (for clocks in a SGI, see [55]), it opens the door for the test of the more complex formulations suggested for the equivalence principle in the quantum domain. Second, as noted in the following works, such an interferometer also opens the door to searches for new physics [56]. Furthermore, such an interferometer is a milestone towards a SGI with nano-diamonds instead of atoms, for a test of quantum mechanics in new regimes and to probe the quantum-gravity interface, e.g., test the quantization of gravity [49]. In addition, such a large-mass interferometer can explore the Díosi-Penrose

conjecture regarding gravitationally-induced collapse, and possible tensions which may arise with the quantum equivalence principle measured in this work (SM).

V. ACKNOWLEDGMENTS

We thank the BGU nano-fabrication facility for the high-quality chip and the BGU support team, especially Menachem Givon, Zina Binstock, Dmitrii Kapusta and Yaniv Bar-Haim for their support in building and maintaining the experiment. Funding: This work was funded, in part, by the Israel Science Foundation (grants no. 856/18, 1314/19, 3515/20, and 3470/21), and the German-Israeli DIP project (Hybrid devices: FO 703/2-1) supported by the DFG. Additional funding was provided by the Gordon and Betty Moore (doi.org/10.37807/GBMF11936), and Simons (MP-TMPS-00005477) foundations. IF thanks an anonymous USA philanthropist, John Moussouris, Jussi Westergren and the Emmy Network for support and research funding. CM and VV thank the Gordon and Betty Moore Foundation and the Templeton Foundation and CM also thanks the Eutopia Foundation, and Ben Vass for supporting her research. W.P.S. is grateful to the Hagler Institute for Advanced Study at Texas A&M University for a Faculty Fellowship, and to Texas A&M AgriLife Research for the support of this work. We thank Časlav Brukner, Daniel Rohrlich, Daniel M. Greenberger, Ernst M. Rasel, Yair Margalit, J. Ströhle, Gary G. Rozenman, Fabio Di Pumbo and Matthias Zimmermann for helpful discussions.

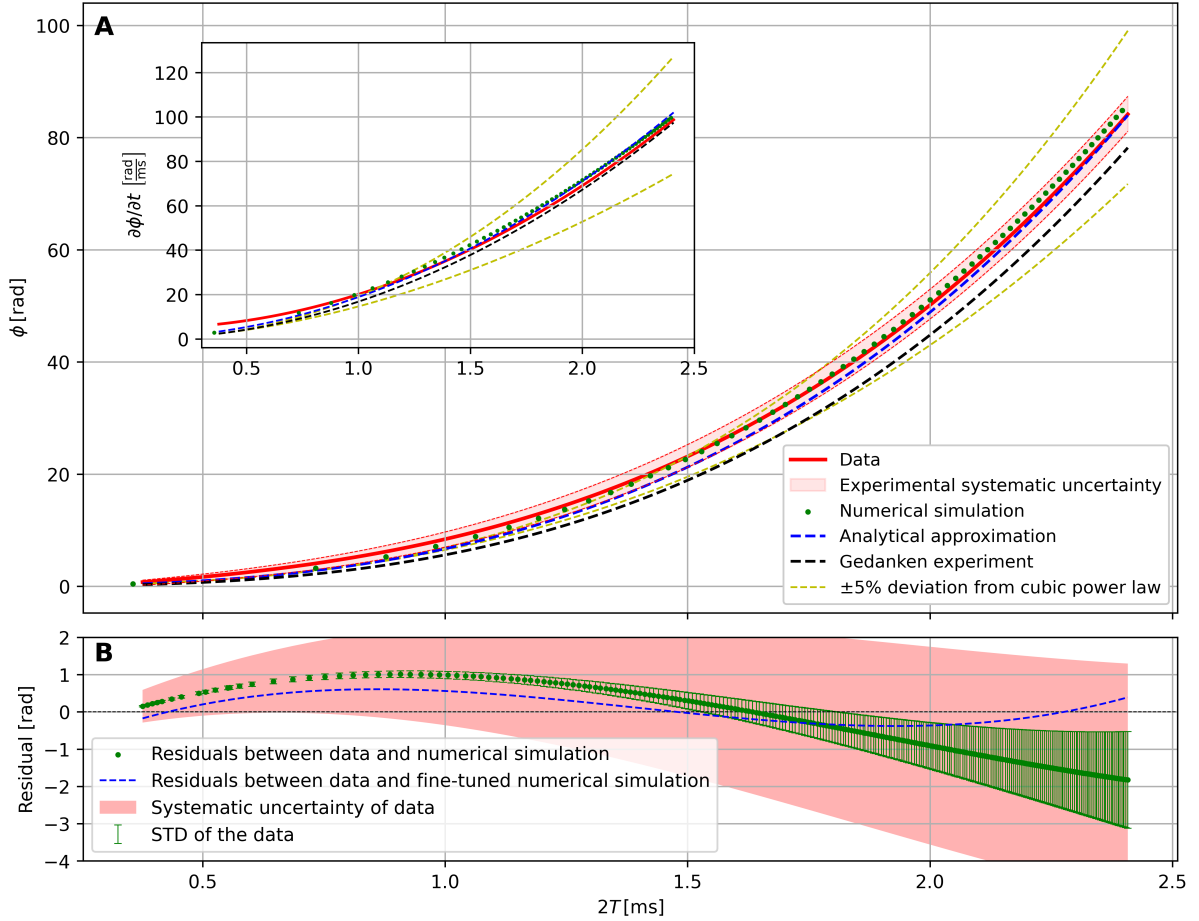


FIG. 3: Phase and its derivative vs. the free-fall duration of the ballistic path $2T$.

(A) The phase difference between the two interferometer arms as a function of the free-fall duration of the upper arm. The red line represents the experimental data, where the phase is extracted from Fig. 2. To estimate the uncertainty bounds, we repeat the experiment with an increase (decrease) of the magnetic-pulse current I_{kick} by 0.5 % (which is our estimated experimental precision) and use the result to plot the upper (lower) uncertainty bounds. The green points are the result of a numerical simulation based on tools we developed for calculating wave packet evolution [52], which include the effects of shape and rotation of the wave packet. The blue dashed line is the result of the analytical approximation of the experiment given in Eq. 4. The analytical model assumes a homogeneous magnetic gradient, and a set of square pulses of current so that the acceleration of each arm is a piecewise constant function. The black dashed line depicts the phase of the *Gedanken* experiment. The inset shows the derivative of the phase with respect to $2T$. To obtain the derivative of the phase for the numeric simulation, we fit a third-order polynomial to the set of points in the main figure and take its derivative. The derivative of the analytical approximation and the *Gedanken* experiment are calculated by direct differentiation. The yellow dashed lines represent 5% deviations from the T^3 phase accumulation model, by modifying the analytical prediction to a power law of $T^{3\pm 0.15}$. This is meant to show that the data is not consistent with such deviations from the cubic phase. (B) The residuals between the phase of the data and the numerical simulation, where the latter is a “blind” simulation with no free parameters or fine tuning. A difference of 2 rad over 13 oscillations spanning a phase of ≈ 80 rad, constitutes a deviation of about 2.5%. The error bars represent the statistical noise of the phase in the experiment, which shows a relative noise of 1.3% of the phase. The red band represents the systematic uncertainties [which also appear in (A)]. The blue line shows the result of the numeric simulation after fine-tuning of the currents and the magnetic field along the z-axis. The kick current is increased by 0.15%, the idle current is changed from 0.55 mA to 0.5 mA, and B_z from 0.33 G to 0.35 G, all within the experimental uncertainties.

VI. METHODS

Let us describe the experimental sequence in some detail (see Fig. 4): we create a ^{87}Rb BEC in the state $|2\rangle \equiv |F = 2, m_F = 2\rangle$ in a magnetic trap produced by current-carrying wires on the atom chip (below the chip which is upside down). We then release the cloud of atoms from the trap and conduct Delta-kick cooling (DKC), which collimates the expansion of the wave packet along the z axis down to an effective temperature of 3.3 nK. As a side effect of this procedure, the atoms are launched upwards (as can be seen on the left side of Fig. 4). The BEC is by now dilute enough so that atom-atom interaction is minimized and the physics becomes single-atom physics. We then apply 100 μs RF pulse transferring atoms to the state $|F = 2, m_F = 1\rangle$. With the help of a $\pi/2$ pulse, each atom is now in a superposition of a magnetic sensitive state $|1\rangle \equiv |F = 2, m_F = 1\rangle$ and a non-sensitive state $|0\rangle \equiv |F = 1, m_F = 0\rangle$. We now apply a magnetic kick which launches the sensitive state upwards. Quickly thereafter, we apply a π pulse, so that the atoms launched upwards are no longer affected by the magnetic gradients and they go into a ballistic trajectory affected only by gravity (up to second order Zeeman). Conversely, the other wave packet becomes sensitive to the magnetic gradient which is now tuned to exactly counteract gravity, so that the wave packet remains stationary in the frame of reference of the laboratory. Finally, we reverse the sequence – apply a π pulse and apply the same SG kick to stop the ballistic wave packet, thus bringing the two wave packets to have the same position and momentum for a full overlap. After one more MW $\pi/2$ pulse, another magnetic gradient kick separates the two spin states in space, so that after some time of flight we are able to determine the population in each output port and consequently in each spin state, and thus measure the output of the interferometer (Fig. 2).

The SG force is created by currents in three parallel gold micro-wires of 2 μm thickness, 40 μm width, separated by 60 μm gaps on the atom chip surface. The current direction in the middle wire is opposite to that in the edge wires, which creates a quadrupole magnetic field with a minimum at approximately 100 μm from the wires. The external magnetic bias field of 12.6 G is applied to suppress spin-flips and introduce a small second-order Zeeman shift for the efficiency of the RF pulse.

The optimal value of the holding current I_{hold} should counteract gravity. To find I_{hold} , we measured trajectories of state $|1\rangle$ with resonant absorption imaging for various values of the holding current (see SM for details) and find $I_{\text{hold}} = 23.07 \pm 1.49$ mA. Although the inaccuracy of gravity compensation is 6.5%, it corresponds to only 0.42% inaccuracy in the phase accumulation, as the deviation from g is introduced squared to the phase (see SM).

The kick currents are set in such a way that the area $\int I(t)dt$ of the two kick current pulses is equal to the area of the holding current pulse for each interferometer duration. In the case of the *Gedanken* experiment and the analytical approximation, such a definition of the kick pulses is equivalent to the condition of full overlap between the wave packets at the end of the interferometer. However, in the real experiment, this condition does not result in perfect overlap due to the curvature of the potential and the finite duration of the pulses. This is quantified in the numerical simulation, where the precise pulse area condition is applied, the two trajectories do not completely overlap at the end, resulting in a small final spatial splitting of 0.2 μm for the largest interferometer duration (as seen in Fig. 5). The effects of rotations and the expansion of the wave packets under the curved potential are also quantified in the numerical simulation and contribute up to 1 rad to the total phase (as seen in Fig. 9). While in Fig. 4 the trajectories produced by an analytical approximation, in Fig. 5 we present several trajectories as they are calculated by the numerical simulation, and as in Fig. 3, the two are in good agreement.

The maximal reached spatial splitting between the two arms is approximately 7.5 μm , based on the numerical simulation and in agreement with the analytical estimations and trajectory imaging.

Next, let us briefly describe the timings of the MW pulses. We use a symmetric dynamical decoupling MW scheme, as it cancels the linear phase due to possible detuning of the MW pulses, improves the coherence time, and reduces the shot-to-shot noise. The rise and fall time of the holding pulse (duration of T_h) are each defined as $\tau_h = 12$ μs . The time between the first and second π pulses defines the MW dynamical decoupling scheme. We define it as $2\tau_{\text{DD}}$, which amounts to $2\tau_{\text{DD}} = 5 + 2 \times \tau_h + T_h + 50$, where 5 μs after the π pulse we start the holding pulse, and 50 μs after the end of the holding pulse we apply the second π pulse (Fig. 4). We then set the time between the $\pi/2$ and π pulses to be τ_{DD} .

Finally, let us describe with a simplified calculation (details in the SM) how the $T_h = 2272$ μs (Fig. 5) or the $2T = 2.4$ ms (Fig. 4) achieve a splitting of about 7.5 μm . We define T_d as the delay between the end of the gradient (kick) pulse and the start of the holding pulse, where 50 μs after the end of the gradient pulse we apply a π pulse (with a duration of 16 μs) that inverts the spin state of the arms so that the bottom arm is now in the magnetically-sensitive state $|1\rangle$, and 5 μs after the π pulse we start the holding pulse. This amounts to $T_d = 50 + 16 + 5 = 71$ μs , where the same delay time appears also after the holding pulse.

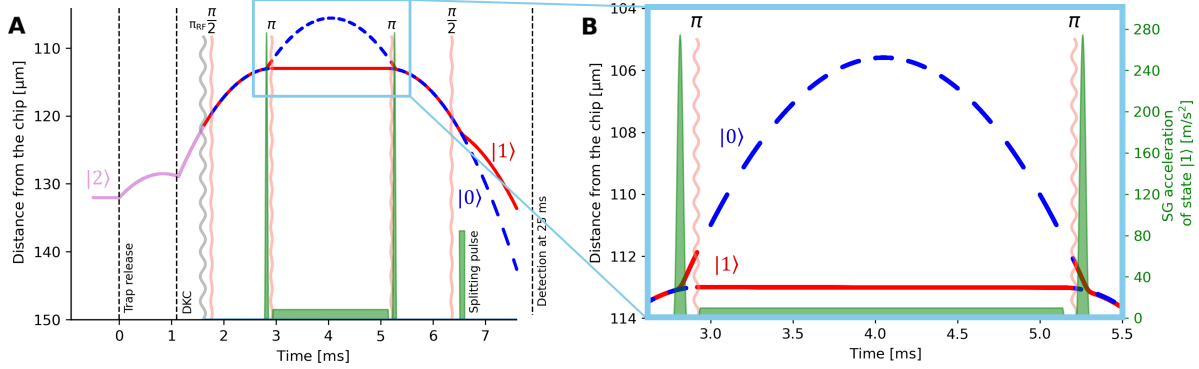


FIG. 4: The experimental scheme and trajectories of the wave packets in the experiment.
 (A) The complete experimental scheme of our longitudinal (1D) QGI, for the case of $2T = 2.4$ ms. The x-axis is time, where we set $t = 0$ at the moment of trap release. At this time the atoms are in the state $|2\rangle \equiv |F = 2, m_F = 2\rangle$. We apply Delta-kick cooling (DKC) at $t = 1.1$ ms, which collimates the wave packet's expansion and launches the atoms into a ballistic trajectory upwards. Before the start of the interferometer, we transfer the atoms to the state $|F = 2, m_F = 1\rangle$ by applying an on-resonance RF π pulse (grey wavy line). During the interferometer, we control the spin state of the atoms with four MW pulses (orange wavy lines) and the momentum of the atoms with three magnetic gradient pulses (green areas). The MW pulses are on resonance with the transition between the $|1\rangle \equiv |F = 2, m_F = 1\rangle$ and $|0\rangle \equiv |F = 1, m_F = 0\rangle$ states, where the $|0\rangle$ state is magnetically non-sensitive in the Zeeman first order. The first $\pi/2$ pulse puts the atoms in an equal superposition of $|1\rangle + |0\rangle$. At the end of the interferometer, the trajectories of these two states are joined to a single trajectory with two spin states, after which the second $\pi/2$ pulse is applied, creating four overlapping wave packets which interfere, two wave packets per each spin state, imprinting the phase difference into a population difference (for simplicity of graphics, we have not differentiated the four wave packets in the plot). After the second $\pi/2$ pulse, we detect the relative population in each state. In the detection scheme, we first spatially separate the states by applying a fourth magnetic gradient and, finally, image the atoms using on-resonance absorption imaging. The symmetric temporal positioning of the $\pi/2$ and π pulses also serves as a dynamic-decoupling scheme, increasing the coherence time, canceling the linear phase accumulation due to possible detuning of the MW and reducing the shot-to-shot phase fluctuations. (B) Zoom-in on the interferometer sequence. The first gradient (kick) pulse applies a maximal acceleration a_{kick} for a total duration of T_{kick} , which launches the top arm into a ballistic trajectory. 50 μ s after the end of the gradient pulse, we apply a π pulse (with a duration of 16 μ s) that inverts the spin state of the arms so that the bottom arm is now in the magnetically-sensitive state $|1\rangle$. 5 μ s after the π pulse, we start the holding pulse (duration of T_h and rise time $\tau_h = 12$ μ s), which applies an acceleration opposite and equal to gravity, to hold the bottom arm stationary in the lab frame. 50 μ s after the holding pulse, we again apply a π pulse and 5 μ s later we recombine the trajectories of the two wave packets by applying a magnetic gradient pulse with a maximal acceleration a_{kick} for a total duration of T_{kick} , as in the first pulse.

The top arm travels $0.5 \times g_{eff} \times (T_{eff})^2 = 7.62 \mu\text{m}$, where $g_{eff} = 9.91 \text{ m/s}^2$ (including acceleration due to the second order Zeeman shift), and $2T_{eff} = T_h + 2 \times \tau_h + 2 \times T_d + T_{kick} = 2T + 80 \mu\text{s}$, is the effective ballistic duration taking into account the translation along z during T_{kick} (only one $T_{kick} = 80 \mu\text{s}$ is added as an average of the two kicks). The bottom arm travels upwards $0.5 \times g_{eff} \times (T_{kick} + T_d)^2 = 0.11 \mu\text{m}$ during T_{kick} and T_d , resulting in a maximal splitting of $7.5 \mu\text{m}$. This is in good agreement with the numerical results presented in Fig. 5.

Full details concerning the experiment may be found in the SM.

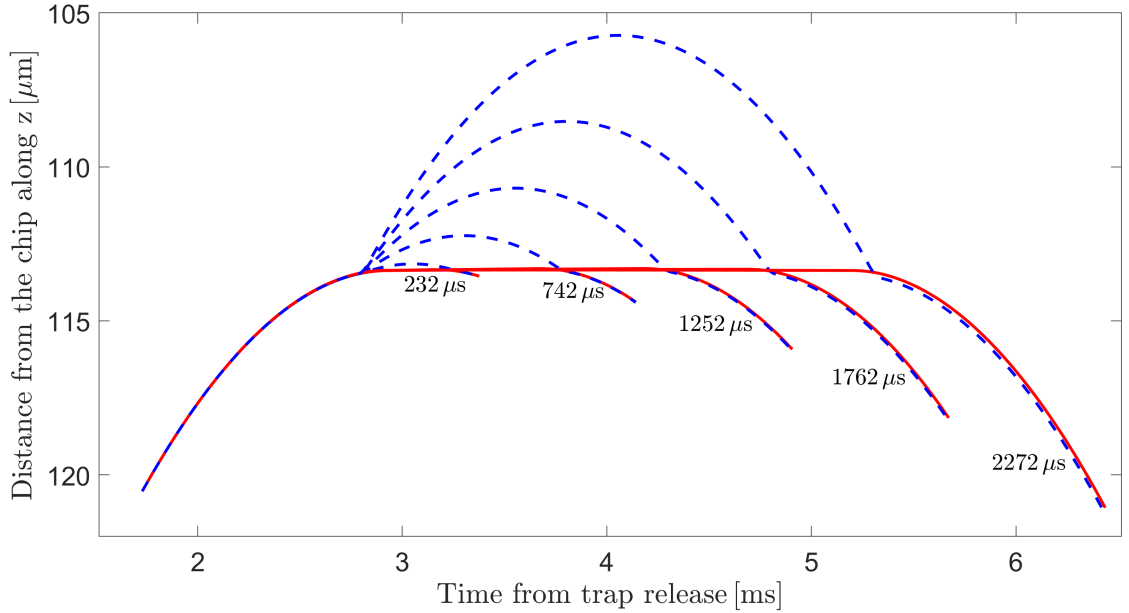


FIG. 5: **The trajectories of the wave packets for different holding durations.**

The trajectories of the two arms of the interferometer, calculated by the numerical simulation for holding durations $T_h = 232, 742, 1252, 1762, 2272 \mu\text{s}$. Dashed blue lines represent the ballistic trajectory, and solid red lines the static wave packet. At the end of the interferometer, a small spatial splitting can be seen, on the order of $0.1 \mu\text{m}$. For $T_h = 2272 \mu\text{s}$, the spatial splitting between the two arms halfway through the interferometer reaches $7.5 \mu\text{m}$. The trajectories are plotted until the time in which the final (second) $\pi/2$ is applied.

VII. SUPPLEMENTARY MATERIAL

A. BEC production

We produce a Bose-Einstein condensate (BEC) of Rb^{87} atoms with $15-30 \cdot 10^3$ atoms in the condensate. To produce the BEC we load atoms from a 2D Magneto-Optical-Trap (MOT) to the 3D-MOT for 5 seconds, with an initial loading rate of $200 \cdot 10^6$ atoms per second and a total of $600 \cdot 10^6$ atoms in the MOT. We compress the MOT and apply optical molasses, and optical pumping, after which we load the atoms to a magnetic trap formed by a copper z-wire. We apply evaporative cooling for 12 seconds and transfer the atoms to the chip trap, where we apply the final evaporation to a BEC for 1 second. At this stage, the current in the y-bias coils is 19 A, and in the x-bias coils 1 A, and the magnetic fields are 12.6 G and 0.7 G, respectively. The chip trap consists of two straight wires with a current of 500 mA and four U-wires with a current of 700 mA, the layout of the wires in the chip is shown in Fig. 6. The trap frequency along the z axis was measured to be 1009 ± 4 Hz, the magnetic field at the trap minimum induced a Zeeman shift of 425 ± 5 kHz.

B. Initial position stability

The phase and visibility of the Stern-Gerlach interferometer (SGI) are sensitive to the initial position of the atoms due to the curvature of the magnetic potential produced by the atom chip wires, thus the stability of the initial position is important both for the shot to shot stability and low frequency drifts. By loading the atoms to the atom chip trap we significantly improve the stability of the initial position compared with the macroscopic z-wire trap. To estimate the stability of the trap position, we measured the shot-to-shot fluctuations of the final position of the trap, resulting in a standard deviation of $0.11 \mu\text{m}$

**Image is not to scale; all dimensions are in microns;
coordinates refer to wire centers; all U wires widths are 200 μm wide**

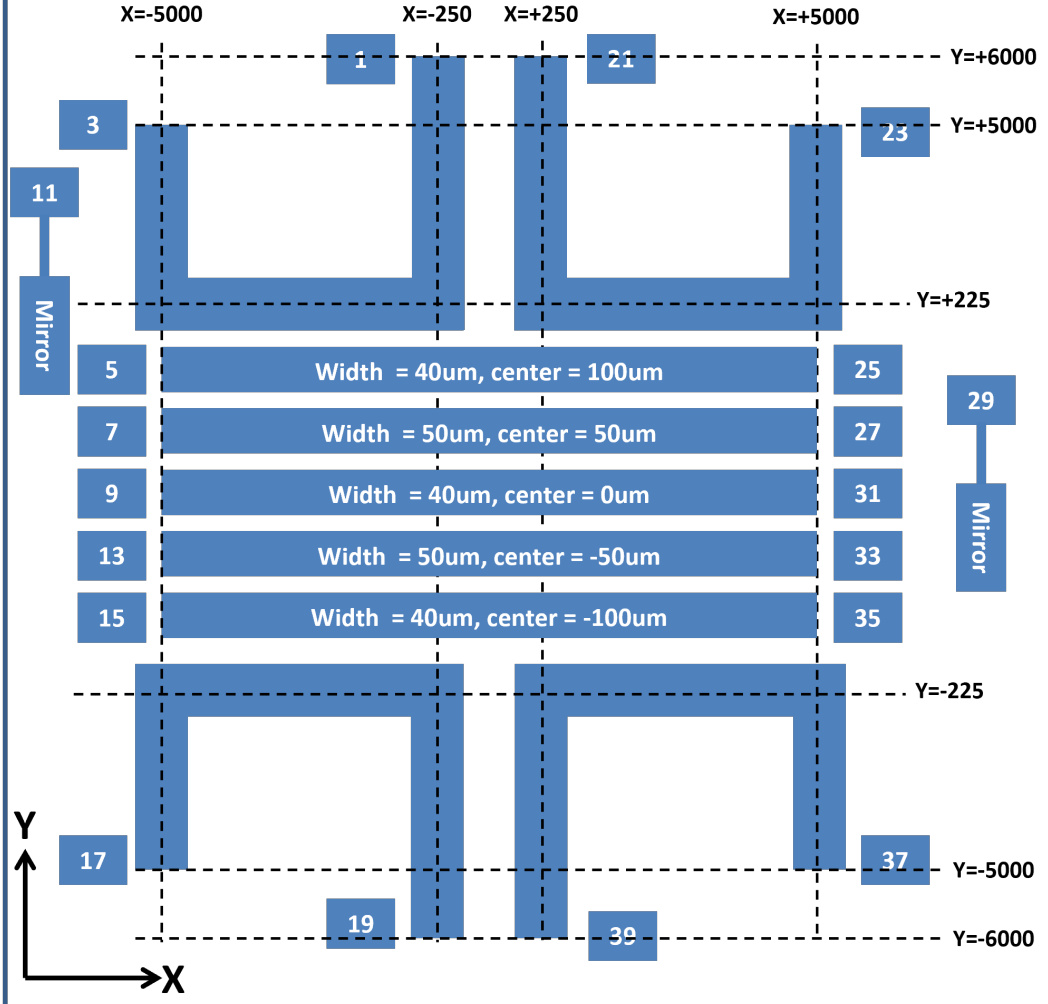


FIG. 6: Schematic representation of the wires on the atom chip. The thickness of the wires is $2 \mu\text{m}$, and their width ranges from $40 - 200 \mu\text{m}$. At the center of the chip are five straight wires. The three SG wires have a width of $40 \mu\text{m}$ each, and their centers are separated by $100 \mu\text{m}$ (labeled 5, 9, 15) with alternating current polarity. The SG wires produce a quadrupole $97 \mu\text{m}$ below the chip surface. The magnetic trap on the chip consists of two straight wires and four U-shaped wires. The straight wires (labeled 7, 13) confine the atoms in the z and y axes and have a width of $50 \mu\text{m}$, and their centers are separated by $100 \mu\text{m}$. The four U-shaped wires confine the atoms along the x-axis and have a width of $200 \mu\text{m}$ each. This confinement is produced by the inner wires (labeled 1, 19, 21, 39).

(see Fig. 7). The high positional stability is a key advantage of the atom chip trap over the z-wire trap, enabling improved visibility, enhanced phase stability, and greater spatial splitting compared to previous experiments [37, 49]. Using the atom chip trap also reduces low frequency noise (drifts) in the interferometer, enhancing the long-term stability of the phase, allowing for long sessions of data taking (3-6 hours of data for one graph), and high repeatability of the experiment.

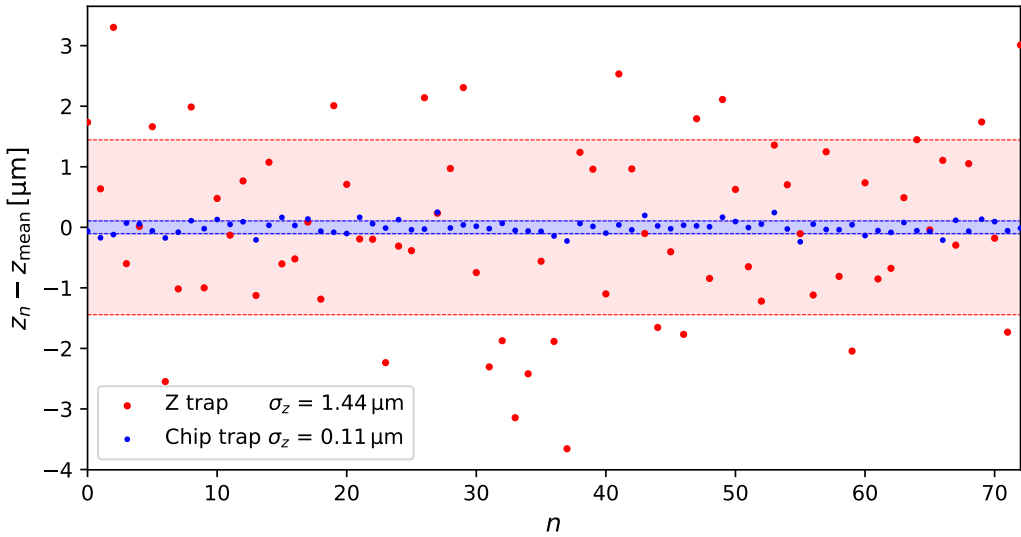


FIG. 7: Initial position stability: Plotting the shot-to-shot fluctuations of the position of the atoms along the z-axis reveals a standard deviation of $0.11\text{ }\mu\text{m}$ in the atom chip trap, compared to $1.44\text{ }\mu\text{m}$ in the z-wire trap. The high stability of the atom chip trap significantly enhances the visibility and phase stability of the SGI.

C. Trap release and Delta-kick cooling

We release the atoms from the trap by shutting off the current in the chip trap with a linear ramp of $30\text{ }\mu\text{s}$. The finite duration of the ramp gives the BEC some momentum upwards. After a time of flight of $1030\text{ }\mu\text{s}$, we apply delta-kick cooling (DKC) by applying a pulse of current in the straight trap wires for $110\text{ }\mu\text{s}$ with a current of 470 mA , (the shape of the pulse is a trapezoid with linear rise of $9\text{ }\mu\text{s}$ and linear fall of $22\text{ }\mu\text{s}$). The DKC collimates the BEC along the z and y axes and reduces its expansion rate to an effective temperature of 3.3 nK along the z axis (see Fig. 8 for a measurement of the temperature with and without DKC). A desired side effect of the DKC is a momentum kick to the BEC that launches it upwards toward the chip. Measurement of this trajectory reveals that the BEC reaches its maximum height $2930 \pm 100\text{ }\mu\text{s}$ after the trap release. The peak of the trajectory is set to be the starting point for the holding pulse.

D. Spin states, MW and RF pulses

We use radio-frequency (RF) and micro-wave (MW) pulses to manipulate the spin state of the atoms. The atoms start in the state $|F = 2, m_F = 2\rangle$, and we apply an RF π pulse, to move the atoms to $|1\rangle = |F = 2, m_F = 1\rangle$, with a frequency of 8.8 MHz and a duration of $100\text{ }\mu\text{s}$. Our two-level system is

$$|0\rangle = |F = 1, m_F = 0\rangle, |1\rangle = |F = 2, m_F = 1\rangle, \quad (5)$$

which we coherently control via MW pulses with a frequency of 6.843 GHz , where the duration of a π pulse is $16\text{ }\mu\text{s}$. The MW scheme consists of four pulses arranged for dynamical decoupling (DD) to reduce environmental effects. The DD scheme consists of four MW pulses $(\pi/2, \pi, \pi, \pi/2)$, with a delay of τ_{DD} between the $\pi/2$ and π pulses, and $2\tau_{DD}$ between the two π pulses, so that the scheme is $(\pi/2, \tau_{DD}, \pi, 2\tau_{DD}, \pi, \tau_{DD}, \pi/2)$. This scheme cancels the linear phase due to detuning, improves the coherence time, and reduces the shot-to-shot noise.

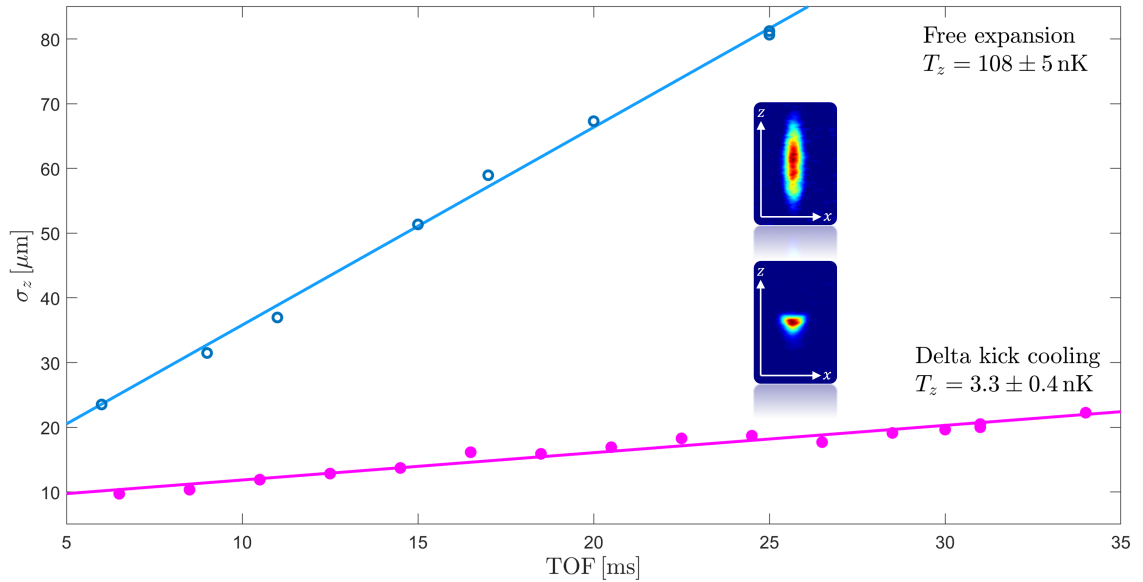


FIG. 8: Temperature measurement along the z axis, with and without DKC. The expansion rate with DKC is $0.4 \mu\text{m}/\text{ms}$, corresponding to a temperature of 3.3nK . For free expansion without DKC the expansion rate is $3.1 \mu\text{m}/\text{ms}$ corresponding to 108nK . The inset shows the CCD image of the atoms with and without DKC after a time of flight of 26.5 ms and 25 ms respectively.

E. Detection

Our detection scheme starts with a strong pulse of magnetic gradient to spatially separate the two different spin states. Once separated into two clouds, we apply absorption imaging with an on-resonance laser tuned to the $F = 2 \rightarrow F' = 3$ transition. To image the atoms in the $F = 1$ state, which is a dark state, we send a pulse of the repumper laser before the imaging laser pulse. The shadow of the atoms is captured on a CCD image from which we analyze the optical density profile, fit it to a 2D-Gaussian, and count the number of atoms in each cloud. When required, we apply a low-pass filter to the image to reduce the noise and improve the signal-to-noise ratio.

F. SGI scheme

We hold one of the two wave packets stationary for a duration T_{hold} applying an acceleration equal and opposite to the gravitational acceleration g . We apply short magnetic gradient pulses with duration T_{kick} to control the second wave packet to launch it into a ballistic trajectory and stop it at the bottom of the trajectory, so that at the end of this sequence, the two wave packets should overlap (up to a small mismatch as shown in Fig. 5) in position and momentum. Between the pulses, we allow a delay time of T_d . In the ideal case, T_{kick} , T_d are very short delta pulses; in an actual experiment, they have a finite length.

Fig. 4 of the Methods section shows the SGI scheme in terms of RF pulses and magnetic gradients and the trajectories of the wave packets. We kick the one wave packet up, allow it to undergo a ballistic trajectory in free fall, and stop it at the end of the trajectory while we hold the second wave packet in place. At each moment, we apply a force only on one arm while the other arm is in a state that is first-order magnetically insensitive ($m_F = 0$) and unaffected by the magnetic gradients (to first-order).

In this scheme, the force from the atom chip is applied while the atoms are located in the quadrupole of the magnetic field produced by the chip or very close to it. This condition reduces the phase noise and improves the stability of the interferometer.

G. Analytical model for calculating the phase

In addition to what has been provided in the main text, let us show how the phase difference between the two arms [Eq. (4) in the main text] is derived by two methods, one using the Gauge transformation [Eq. (1) of the main text], and the second using the action (Secs. G.1 and G.2, respectively). In both these derivations the analytical model approximates the experiment as a set of square pulses of a homogeneous magnetic gradient so that the acceleration of each arm is a piecewise constant function. In Sec. G.3, we calculate the action of each of the arms from the perspective of both frames, and finally, in Sec. G.4, we show how the result may be obtained using the Galilean transformation.

1. Derivation of the phase difference using the Gauge transformation

The transformation between an Einsteinian and Newtonian frames of reference [Eq. (1) of the main text] can be generalized to represent a transformation between any frame without forces and a frame with a constant acceleration \mathbf{a} , such that

$$\psi_N(\mathbf{r}, t) = e^{i\phi_{\text{gauge}}(\mathbf{r}, t)} \psi_E(\mathbf{r} - \frac{1}{2}\mathbf{a}t^2, t), \quad \text{with} \quad \phi_{\text{gauge}}(\mathbf{r}, t) = \frac{m}{\hbar}[-\frac{1}{6}a^2t^3 + \mathbf{a} \cdot \mathbf{r}]. \quad (6)$$

Here it is assumed that both frames have the same velocity at $t = 0$ and the zero point for the energy is taken to be at $\mathbf{r} = 0$.

First we explain the phase difference in the *Gedanken* experiment [Eq. (2) of the main text], from the gauge transformation. We take the time $t = 0$ to be at the middle point where the ballistic path is at the turning point. In the frame falling with this path the velocity at this point is equal to the velocity of the Newtonian (lab) frame ($v = 0$ in the lab frame). At the two end-points $t = \pm T$ this frame has a velocity $\mp v_0 = \mp gT$ and to fulfil the closing condition the center of the wave packet at these times should be at the same position of the reference path, which we may choose to be $z = 0$. In addition, at these points we apply a kick $v_0 = gT$, which amounts to adding a phase term $e^{\pm imv_0 z/\hbar} = e^{\pm imgTz/\hbar}$ (at $t = -T$ this phase is negative, as the closing condition is reversed in time). This phase cancels the phase in the second term of Eq. (1), but it is anyway canceled for the phase at the wave-packet center, which is at $z = 0$ at this time.

While Eq. (2) of the main text refers to the phase accumulated by the ballistic path during the free-fall time and represents the full interferometer phase in the *Gedanken* experiment, we can also use the same transformation in Eq. (6) to derive the total phase difference between the two paths in a model that includes the finite duration of the kick pulses T_{kick} , and the delay time T_d . In the analytical model that was used in Fig. 3 we model the gradient pulses in the sequence by square pulses: a kick pulse of duration T_{kick} applied to the ballistic wave packet, followed by a delay time T_d before the holding pulse of duration $T_h = 2T - 2T_d$ is applied to the reference wave packet. The holding time is followed by another delay time T_d and a kick pulse of duration T_{kick} , such that the reference wave packet is in free fall during the two time intervals of duration $T_{\text{kick}} + T_d$ before and after the holding time. We assume that the reference path is completely at rest during the holding time at a constant position $z = 0$. It follows that the phase accumulated during the holding time is zero. In order to obtain the phase accumulated during the free-fall time of the reference wave packet before the holding time we set the time $t = 0$ to be just before the beginning of the holding pulse. The gauge phase at this $t = 0$ is 0, and the phase comes from the gauge phase at the beginning of the first kick pulse, where the wave packet is centered at $z_0 = -g(T_{\text{kick}} + T_d)^2/2$ and we obtain the phase that the reference wave packet accumulated during the first free-fall interval

$$\phi_{\text{ref}}^{(\text{free})} = -\phi_{\text{gauge}}(z_0, -T_{\text{kick}} - T_d) = -\frac{m}{\hbar} \left[\frac{1}{6}g^2(T_{\text{kick}} + T_d)^3 + gz_0(T_{\text{kick}} + T_d) \right] = \frac{mg^2}{3\hbar}(T_{\text{kick}} + T_d)^3. \quad (7)$$

An equal phase is obtained from the gauge phase during the second free-fall interval of the reference path and we obtain

$$\phi_{\text{ref}} = \frac{2m}{3\hbar}g^2(T_{\text{kick}} + T_d)^3. \quad (8)$$

The phase accumulated by the ballistic wave packet during the kick pulse can be calculated by using the transformation from a frame that is accelerated by $\mathbf{a} = (a_{\text{kick}} - g)\hat{z}$, where $a_{\text{kick}} = g(T - T_d)/T_{\text{kick}}$ that

satisfies the closing conditions that require that the integrated acceleration applied to the reference wave packet during the holding time $2(T - T_d)$ should be equal to the integrated acceleration of the ballistic wave packet. For applying this transformation by using Eq. (6) we need to set the initial time $t = 0$ to be the time where the velocity is zero in the lab frame under the same acceleration. The velocity at the beginning of the first kick pulse is given by $v(t_0) = g(T_{\text{kick}} + T_d)$ and therefore the velocity is zero when $t = t_0 - v(t_0)/(a_{\text{kick}} - g) = t_0 - \frac{g}{a_{\text{kick}} - g}(T_{\text{kick}} + T_d) = 0$. At the end of the kick pulse the position of the wave-packet center is at $z_1 = z_0 + g(T_{\text{kick}} + T_d)T_{\text{kick}} + \frac{1}{2}(a_{\text{kick}} - g)T_{\text{kick}}^2$ and we obtain for the phase

$$\phi_{\text{kick}} = \frac{m}{\hbar} \left\{ \frac{1}{6}(a_{\text{kick}} - g)^2[(t_0 + T_{\text{kick}})^3 - t_0^3] + (a_{\text{kick}} - g)[z_1(t_0 + T_{\text{kick}}) - z_0 t_0] \right\}. \quad (9)$$

An equal phase is accumulated during the second kick pulse. The phase accumulated by the ballistic path during the free fall has to be changed with respect to the expression of the *Gedanken* experiment such that the term linear in time in Eq. (6) is also included, as in general $z_1 \neq 0$. We then have

$$\phi_{\text{ballistic}}^{(\text{free})} = 2 \frac{m}{\hbar} \left[-\frac{1}{6}g^2 T^3 - g z_1 T \right]. \quad (10)$$

When we combine the results of the above equations and substitute for the value of a_{kick} to fulfill the closing condition we finally obtain

$$\begin{aligned} \Delta\phi &= 2\phi_{\text{kick}} + \phi_{\text{ballistic}}^{(\text{free})} - \phi_{\text{ref}} \\ &= -\frac{mg^2}{3\hbar} (T^3 + T^2 T_{\text{kick}} + T(T_{\text{kick}}^2 + T_d T_{\text{kick}}) - T_d(T_{\text{kick}} + T_d)^2), \end{aligned} \quad (11)$$

which is the same result as in Eq. (4) of the main text (with an opposite sign due to the fact that the phase in the main text was defined such that it grows positively with the time T).

2. Derivation of the phase difference using the action

Alternatively, to calculate the phase of the interferometer in the common method, we use the action of the classical path

$$\phi_j = \frac{1}{\hbar} S_j = \int_0^{t_f} [K_j(t) - U_j(t)] dt, \quad (12)$$

where j is an index of the respective interferometer path, and

$$K_j(t) = \frac{1}{2}mv_j^2(t), \quad U_j(t) = -m(g + a_j)z_j(t). \quad (13)$$

To maintain the symmetry of the trajectories we set the initial conditions of the COM of the wave packet to be

$$v_z(0) = g(T_{\text{kick}} + T_d) \quad ; \quad z(0) = -g(T_{\text{kick}} + T_d)^2/2 \quad (14)$$

We define the total interferometer time as $2T + 2T_{\text{kick}}$, and the holding duration of the bottom arm can be defined as $T_h = 2T - 2T_d$. The experiment can be described by a set of durations $(T_{\text{kick}}, T_d, T_h, T_d, T_{\text{kick}})$, where the acceleration of the ballistic and reference paths in each of these durations is given by $a_{\text{ballistic}} = -g + (a_{\text{kick}}, 0, 0, 0, a_{\text{kick}})$ and $a_{\text{reference}} = -g + (0, 0, a_{\text{hold}}, 0, 0)$. The condition for a closed interferometer is $a_{\text{kick}} = \frac{g}{2T_{\text{kick}}}T_h$ and setting $a_{\text{hold}} = g$ confirms that the reference path is stationary in the lab frame. Performing the integrals, we get

$$\phi_1 = \frac{mg^2}{3\hbar} (-T^3 - T^2 T_{\text{kick}} - T T_{\text{kick}}^2 - T T_{\text{kick}} T_d + 2T_{\text{kick}}^3 + 7T_{\text{kick}}^2 T_d + 8T_{\text{kick}} T_d^2 + 3T_d^3) \quad (15)$$

$$\phi_2 = \frac{2mg^2}{3\hbar} (T_{kick} + T_d)^3 \quad (16)$$

$$\Delta\phi = \frac{mg^2}{3\hbar} \left(T^3 + T^2 T_{kick} + T (T_{kick}^2 + T_{kick} T_d) - T_d (T_{kick} + T_d)^2 \right). \quad (17)$$

Taking the limit of a short kick we get

$$\lim_{T_{kick} \rightarrow 0} \Delta\phi = \frac{mg^2}{3\hbar} (T^3 - T_d^3). \quad (18)$$

and the limit of short delay we get

$$\lim_{T_{kick}, T_d \rightarrow 0} \Delta\phi = \frac{mg^2}{3\hbar} T^3. \quad (19)$$

The result of the analytical model is given here in Eq. (17) (and in Eq. (7) of the main text) is plotted in Fig. 3 of the main text using the experimental values of $T_{kick} = 80 \mu\text{s}$ and $T_d = 71 + 6 \mu\text{s}$ where we include half the rise time of the holding pulse $\tau_{\text{hold}}/2 = 6 \mu\text{s}$ in the delay. In the analytical model prediction, we also include the effect of the second-order Zeeman energy of the $|0\rangle$ state. This energy results in a small force on the $|0\rangle$ state during the gradient pulses, approximately 1% of the force on the $|1\rangle$ state, and in the opposite direction. To account for this second-order effect, we calculate the acceleration of the $|0\rangle$ state due to second order Zeeman effect during the holding stage $a_{\text{SOZ}} = 0.10 \text{ m/s}^2$ (see Sec. K for calculation of a_{SOZ}). We set $g_{\text{eff}} = g + a_{\text{SOZ}} = 9.91 \text{ m/s}^2$ in the analytical prediction. Accounting to a_{SOZ} by setting $g_{\text{eff}} = g + a_{\text{SOZ}}$ is accurate up to the leading order of T , and comparing the analytical model that includes a_{SOZ} explicitly to setting $g_{\text{eff}} = g + a_{\text{SOZ}}$ shows that the two agree up to 0.03 rad.

The *Gedanken* experiment is the case of the simple thought experiment, in which the kick pulse is a delta pulse so that $T_{kick} = 0$, and the technical delay between the pulses vanishes setting $T_d = 0$. The prediction is given by setting $T_{kick} = 0$ and $T_d = 0$ in Eq. 15 (or 6) which results in Eq. 19.

An analytical calculation can also include the temporal shape of the pulses and account for time-dependent homogeneous magnetic pulses. However, for the scope of this paper, we choose to show the analytical case only for the more straightforward case of piecewise constant acceleration and use the numerical simulation to include the temporal and spatial modulation of the gradients.

3. Calculating the actions in both frames

Next, to understand the symmetry of the QGI, as emphasized in the introduction, we calculate for the *Gedanken* experiment the actions associated with the classical trajectories of the reference and the ballistic wave packets as seen from both frames of reference, keeping track of the contributions from the kinetic and potential energies as well as the pulses, which we model for the sake of simplicity by delta functions.

We start by discussing the situation in the Newtonian frame. Here the reference wave packet remains at rest for all times, since the gravitational acceleration g is compensated by the acceleration a provided by the magnetic field gradient. Hence, the contributions due to the kinetic and potential energies vanish. Moreover, there are no pulses. Thus, the total action of the reference wave packet vanishes as indicated in Table I.

In contrast, two parts contribute to the total action of the ballistic wave packet. Due to the non-vanishing momentum mv_0 of the atom originating from the first pulse, the accelerated motion in the linear gravitational potential provides us with non-vanishing actions due to the kinetic as well as the potential energies. Their structure shown in the second row of Table I becomes apparent when we recall that the velocity of this motion consists of the constant velocity v_0 and the one caused by the gravitational acceleration g . The action due to this kinetic energy involves the integral of the square of this time-dependent velocity creating the sum of three terms: (i) The kinetic energy $mv_0^2/2$ multiplied by the interferometer time $2T$. (ii) A cross term between the velocity v_0 and the acceleration g and (iii) the square of the acceleration times $(2T)^3$.

Moreover, we emphasize that each term has an interesting combination of v_0 , g and T . Indeed, the term proportional to v_0^2 is linear in T but independent of g . The cross term is linear in v_0 and g but quadratic in T , and the third contribution is independent of v_0 but quadratic in g and cubic in T .

This scaling in v_0g and g^2 is crucial for the equivalence principle. Indeed, when we replace v_0 by $-v_0$ and g by $-a$ as defined by the Einsteinian frame discussed in the second column of Table I, the expressions, now occurring for the reference rather than the ballistic wave packet, are identical.

Next we turn to the contribution from the potential energy of the ballistic wave packet in the Newtonian frame. Since the ballistic wave packet starts from the origin of the coordinate axis, the motion is a combination of the linear motion due to v_0 , and the gravitational acceleration g giving rise to two terms in the action which are identical in size and sign to the last two terms of the action due to the kinetic energy. Hence, these terms also satisfy the symmetry in v_0g and g^2 .

It is interesting that in the Newtonian frame the delta function pulses do not contribute to the actions of the ballistic wave packet in the Newtonian frame, and this for two reasons: First, the corresponding potential energy is proportional to the coordinate at the time of the pulse and second, the ballistic wave packet starts at $z = 0$ and concludes its journey at $z = 0$.

As a result, the total action of the ballistic wave packet is given by the ones of the kinetic and potential energies which due to the closing condition connecting v_0 and T allows us to combine the three terms in a single one shown in the Table I, determining the difference of the actions corresponding to the two wave packets.

Finally, we address the Einsteinian frame which is attached to the motion of the ballistic wave packet. As mentioned before, the two wave packets exchange their roles compared to the Newtonian frame. Hence, now the action of the ballistic wave packet vanishes but the one of the reference wave packet is non-vanishing arising from the magnetic field gradient in the same way as for the ballistic wave packet in the Newtonian frame.

Moreover, the symmetry of the terms discussed before, ensures that the origin of this contribution is identical to one of the terms of the ballistic wave packet in the Newtonian frame.

Since we consider the difference of the actions of the two wave packets there must be a sign difference between the two frames. Indeed, in the Newtonian frame the action of the reference wave packet vanishes, whereas for the Einsteinian frame it is that of the ballistic wave packet.

4. Derivation of the phase difference using Galilean transformation

Finally, we rederive the phase difference measured by the QGI using the combination of the Galilean transformation and the one into freely-falling frame, given by Eq. (1) of the main text. For this purpose, we first recall the Galilei transformation [57]

$$\psi_N(z, t) = e^{i\varphi(z, t)} \psi_0(z - v_0 t, t), \text{ where } \varphi(z, t) \equiv \frac{m}{\hbar} \left(-\frac{1}{2} v_0^2 t + v_0 z \right) \quad (20)$$

between the time-dependent wave functions in the Newtonian frame and in the frame moving with the constant velocity v_0 . Due to the momentum transfer $p_0 = mv_0$ onto the initial wave packet $\psi_0(z, 0)$, the particle is at rest in this frame but undergoes free quantum dynamics.

To include the gravitational acceleration, we combine Eq. (1) and Eq. (20) which yields

$$\psi_N(z, t) = e^{i\phi_{gauge}(z, t)} e^{i\varphi(z + \frac{1}{2}gt^2, t)} \psi_0 \left(z - v_0 t + \frac{1}{2}gt^2, t \right). \quad (21)$$

We now consider the wave function ψ_N at $t = 2T$ and use the closing condition $T = v_0/g$. As a result, the spatial argument in ψ_0 reduces to z . Moreover, the second pulse employed at $t = 2T$ imprints again the momentum p_0 onto the wave function, resulting in

$$\psi_N(z, 2T) = e^{i\phi_{ballistic}} \psi_0(z, 2T), \quad (22)$$

where we have introduced the ballistic phase

$$\phi_{ballistic} = -\frac{1}{3\hbar} mg^2 T^3. \quad (23)$$

TABLE I: Contributions to the actions of the center-of-mass motion of the reference and the ballistic wave packets in the QGI viewed from the Newtonian and the Einsteinian frames. Note that the closing conditions to obtain the respective total actions are written in round brackets whereas the levitation condition for the respective difference in actions are given by the expression in square brackets. In the Newtonian frame the reference wave packet is levitated and remains at rest at the origin. The Einsteinian frame is attached to the ballistic wave packet. Thus, in this frame the wave packet remains at rest at the origin yielding only vanishing actions. This is also the case for the reference wave packet but in the Newtonian frame.

actions	frame	Newtonian	Einsteinian
reference wave packet	kinetic	0	$mv_0^2 T - 2mv_0 aT^2 + \frac{4}{3}ma^2 T^3$
	potential	0	$-2mv_0 aT^2 + \frac{4}{3}ma^2 T^3$
	pulses	no pulses	0
	total	0	$-\frac{1}{3}ma^2 T^3$ ($v_0 = aT$)
ballistic wave packet	kinetic	$mv_0^2 T - 2mv_0 gT^2 + \frac{4}{3}mg^2 T^3$	0
	potential	$-2mv_0 gT^2 + \frac{4}{3}mg^2 T^3$	0
	pulses	0	no pulses
	total	$-\frac{1}{3}mg^2 T^3$ ($v_0 = gT$)	0
difference in total actions		$-\frac{1}{3}mg^2 T^3$	$\frac{1}{3}ma^2 T^3$ [$a = -g$]

H. Numerical simulation

1. Details of the numerical simulation

The numerical simulation calculates the dynamics of the atomic BEC during the trapping, release, DKC and the interferometer sequence. The simulation is based on the model of wave packet evolution given in [52] which is extended to include the effects of rotations. To use the model with curved magnetic potentials, we locally approximate the magnetic potential by a quadratic potential and calculate the evolution of each wave packet in the potential. The simulation predicts the output of the SGI by calculating the overlap integral of the two final wave packets, resulting in a complex value, where the visibility is the magnitude of this integral and the phase is the argument.

The simulation is constructed to mimic the exact experimental sequence by using the same timings as in the experiment. During the preparation stage, the currents and magnetic fields in the simulation are kept close to the values reported in the experiment but fine-tuned to match the wave packet's initial conditions, such as initial position and velocity and initial expansion rate. As the measurements of the absolute positions of the atoms are accurate up to a few μm , other indications of the position of the atoms in the lower interferometer arm are also taken from the holding current required to hold the atoms against gravity, and the ballistic trajectory after the DKC. A holding current of 23-24 mA corresponds, according to the calculation, to a distance of 112-113 μm from the chip surface. The position of the initial magnetic trap is estimated from the ballistic trajectory after the DKC; assuming that the velocity of the atoms at this position before turning on the holding pulse is almost zero, we can deduce the trajectory

after the DKC as the atoms are in free fall and hence travel a distance $\Delta z = \frac{1}{2}gt^2$. This calculation indicates a distance of about $132\ \mu\text{m}$ from the chip surface for the initial trapping position. These values agree with direct measurements of the atomic positions.

The magnetic bias field is taken to be the field generated by the bias coils and Earth's magnetic field $\mathbf{B}_E = (-0.31, 0, 0.33)\ \text{G}$. The bias generated by the coils consists of a component in the y direction and in the x direction, which are determined to be $B_{0y} = 12.9928\ \text{G}$ and $B_{0x} = -1.175\ \text{G}$. The y -component of the field during the trapping determines the trap position with respect to the chip surface and the x -component determines the trap frequency and field at the bottom of the trap. The total magnetic field magnitude is indeed measured some time after trap release by the RF transition frequency between the Zeeman levels $|2, 2\rangle$ and $|2, 1\rangle$. This measurement indicates that the total field at this time is $B_0 = 12.625\ \text{G}$, but we take the field during the trapping to be $B_0 = 13.05\ \text{G}$ to ensure that the trapping position is about $132\ \mu\text{m}$ from the chip surface, which is consistent with the position of the atoms in the lower arm of the interferometer, as described above. The discrepancy between the measured bias field after the trap release and the predicted bias field required to explain the trapping stage may be explained due to the weak magnetic response of the atom chip mount and the chamber itself, resulting in transient fields in the science chamber during the trapping. Time dependence of the bias field after the trap release and DKC is observed in the RF resonance measurements. The z -component of the magnetic field generated by Earth is responsible for a shift of the trapping position relative to the center of the system and we find numerically that the trapping position is at $\mathbf{r}_{\text{trap}} = (0.79, 4.67, 132.05)\ \mu\text{m}$ relative to the center of the surface of the central wire. The trapping frequencies are $\omega_y \approx \omega_z \approx 2\pi \times 1.04\ \text{kHz}$ and $\omega_x \approx 2\pi \times 57\ \text{Hz}$, which is in good agreement with the measured trap frequencies. The calculated field at the bottom of the trap is $B_0 \approx 0.825\ \text{G}$, which is a bit larger than the measured value. For a total number of $2 \cdot 10^4$ atoms we obtain a BEC of an average width $\sigma_x = 3.13\ \mu\text{m}$ in the longitudinal direction and $\sigma_y = \sigma_z = 1.31\ \mu\text{m}$ in the transverse direction. This serves as the starting point for calculating the evolution of the wave packet widths during the sequence. The constant bias field also includes a measured gradient $B' = 68.32\ \text{G/m}$, giving rise to an acceleration $\mu_B B'/2m = 0.22\ \text{m/s}^2$ in the direction of gravity. The DKC pulse kicks the atoms upwards and after it the atoms are in free fall until the beginning of the interferometer, except that they are affected by small magnetic gradients from the bias field and an idle current from the kick wires on the chip. During this time they are transferred from the state $|2, 2\rangle$ to the state $|2, 1\rangle$ by a RF pulse that ends about $400\ \mu\text{s}$ after the collimation pulse and then they are split into a superposition of $|2, 1\rangle$ and $|1, 0\rangle$. As the idle current is designed to counteract the magnetic gradient of the bias during the time between the splitting $\pi/2$ pulse and the recombining $\pi/2$ pulse we may consider the trajectory of the atoms before the kick pulse as being ballistic and calculate the timing and position of the turning point where the atoms are expected to have a zero velocity. This point is given by $z_h = \frac{1}{2}gt^2$, where t is the time between the end of the kick pulse and the turning point. At this point the holding current I_h is calculated and the kick current I_k is also calculated such that the holding current and kick currents satisfy $2I_kT_k = I_hT_h$. The DKC is optimized to yield a zero velocity of the atoms at the beginning of the holding pulse such that the lower trajectory is constant during the holding time. The ballistic trajectory is calculated based on the calculated kick current and the second-order Zeeman effect is taken into account during the holding time of the lower arm, as well as the effect of the second-order Zeeman over the whole sequence.

The free parameters of the simulation are the bias field in the x and y directions and the exact value of the collimation current. By varying these parameters while keeping a flat lower arm trajectory around the correct distance from the chip surface we calculate a phase uncertainty that grows linearly to a maximum/minimum uncertainty of about ± 0.07 radians at the longest holding times included in the experimental results. Note that these parameters were not used for fitting the phase but rather to fit other parameters of the sequence so that the numerical simulation curve in Fig. 3 can be considered as a curve without fitting parameters related to the phase.

In addition, the second simulation curve [blue line in Fig. 3(B)] represents an attempt to best fit the experimentally measured phase without exceeding the uncertainty range of the parameters. In the latter simulation the holding current was taken to be $23.5\ \text{mA}$ (although a larger current was required to hold the reference arm against gravity) and the DKC current was taken to be $0.4705\ \text{mA}$ (instead of $0.4695\ \text{mA}$ for the first simulation). The kick current was taken larger by 0.15% , the idle current was taken to be $0.5\ \text{mA}$ instead of $0.55\ \text{mA}$ and B_z was taken to be $0.35\ \text{G}$ instead of $0.33\ \text{G}$. All these changes are well within the uncertainty limits of the experimental parameters.

2. Effect of wave packet shape on the phase

The numerical simulation includes the effect of the wave-packet shape, which evolves due to single particle effects (internal kinetic energy at the wave-packet center and response to the curved potentials) and atom-atom interactions. To estimate the effects of the wave-packet shape on the phase, we compare the total phase calculated from the overlap integral to the phase of the classical trajectory of the COM. The result is shown in Fig. 9. The total phase accumulation in the experiment amounts to 80 rad while the contribution due to the shape of the wave packet is in the range of 0 to 1 rad. The relative contribution of the “non trajectory” phase is as high as 7% for short interferometer durations, but reduces for longer interferometer times. The exact contribution due to the shape of the wave packet depends on the exact shape of the wave packet and the specific experimental conditions, and can be one of the sources of the discrepancy between the numerical simulation and the experimental data. The numerical simulation also includes the effect of the ambient gradient in the chamber, which was measured to be 0.7 G/cm (equivalent to an acceleration of 0.2 m/s² along gravity of the $|1\rangle$ state, see Sec. L for more details) and the idle current of 0.55 mA we apply to counteract the effect of the ambient gradient. The shape of the pulses of current in the SG wires is also included in the simulation. A detailed description of the pulses is given in Sec. J.

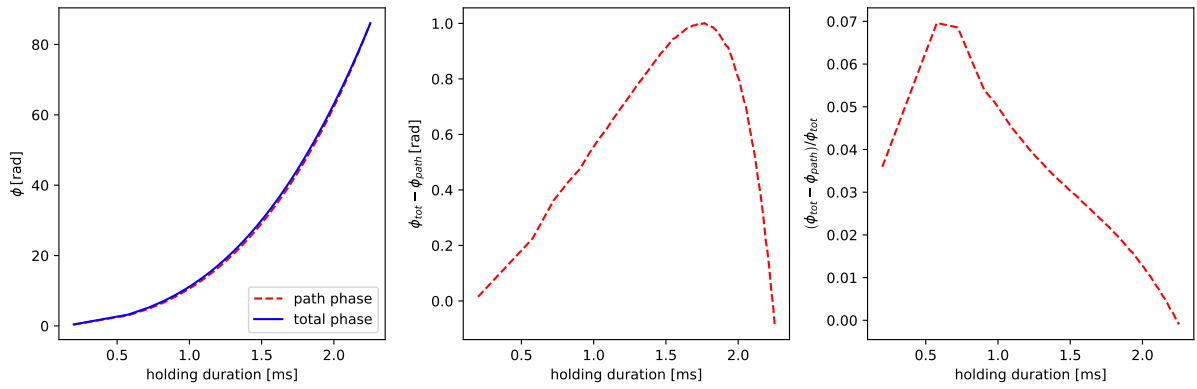


FIG. 9: The different phase contributions calculated in the numerical simulation. (A) The total phase (blue solid line), was calculated from the overlap integral between the two wave packets at the end of the interferometer (the timing of the last $\pi/2$ pulse). This total phase takes into account effects of wave packet shape and atom-atom interaction. The red dashed line is the “path phase”, the phase accumulation due to the classical trajectory of the COM. (B) The difference between the two calculations, shows that the “non trajectory” contributions range between -1.1 to 0.4 rad, out of the total 80 rad of the interferometer. (C) The relative part of the “non trajectory” is as high as 15% for short interferometer duration, but reduces to less than 2% for durations longer than 1.2 ms.

I. Data analysis for figures 2 and 3

To extract the phase from the raw data of population vs. time, we fit the data to a model $P = P_{\text{mean}}(2T) + \frac{1}{2}V(2T) \cos [\phi(2T)]$, where V is the visibility of the oscillations, ϕ is the phase of the oscillations and P_{mean} is the mean value of the population. To obtain the fit, we first identify the upper and lower envelopes and fit them to a polynomial to get P_{mean} and $V(2T)$. We then fit the data to the model where the phase $\phi(2T)$ is a third-order polynomial. During the fitting we exclude the first and last oscillation as they suffer from larger uncertainty in the values of the envelope. As fitting such a model to the data requires a good initial guess, we use the Hilbert transform [58, 59] to extract the phase from the data. The details of the analysis are given below.

1. Figure 2 - Extracting the phase and fitting the data

We fit the data of population vs. time with the following algorithm: First, we fit the envelope of the oscillations by finding the local maxima (minima), connecting them with a set of straight lines, and fitting them to a polynomial. For the data in Fig. 2, a polynomial of order seven was used for the envelopes. Once we have an equation for the upper and lower envelope, we calculate the local amplitude $V/2(2T)$ and local mean $P_{mean}(2T)$. We then apply the Hilbert transform, which results in a complex number for each data point, whose argument is the phase up to $2\pi n$, so we unwrap the phase of the whole data, which requires high enough sampling rate in each oscillation. At this point, we fit a third-order polynomial to obtain a smooth function $\phi(2T)$. We use this polynom as the initial guess for the final fit on the population. While the Hilbert transform is a powerful tool for extracting the phase, it introduces significant edge effects, which are hard to avoid. The direct fit of the phase to the data is more robust to edge effects, and is used for the final fit of the data.

2. Figure 3

In Fig. 3(A), we show the phase derived from the experimental data against three calculations of $\phi(2T)$: the numerical simulation, the analytical approximation and the expected phase in the *Gedanken* experiment. We calculate the lines of the analytical approximation and the *Gedanken* experiment using Eq. 4 and Eq. 19 respectively. The line of experimental data was derived by a fit to the data of Fig. 2 (as explained above), and the data points of the numerical simulation were derived as explained in Sec. H. We also plot as a guide to the eye deviations from the T^3 phase accumulation, by plotting a modified version of the analytical approximation,

$$\Delta\phi = \frac{mg^2}{3\hbar} \left(\frac{mg^2}{3\hbar}^{\frac{\alpha}{3}} T^{3+\alpha} + T^2 T_{kick} + T (T_{kick}^2 + T_{kick} T_d) - T_d (T_{kick} + T_d)^2 \right), \quad (24)$$

where we set $\alpha = 0.15$ to show 5% deviation from the T^3 phase accumulation, and the coefficient $\frac{mg^2}{3\hbar}^{\frac{\alpha}{3}}$ is added to maintain the correct units. As mentioned in the main text, to estimate the uncertainty bounds, we repeat the experiment with an increase (decrease) of the magnetic-pulse current I_{kick} by 0.5 % (which is our estimated experimental precision) and use the result to plot the upper (lower) uncertainty bounds. The inset shows the rate of phase accumulation $\frac{\partial\phi}{\partial t}$, of the same four cases. To get the derivative of the phase for the numerical simulation, we fit a third-order polynomial on the set points and calculate the analytical derivative of the polynomial. For the experimental data we use the analytical derivative of the polynomial found in Fig. 2. The derivative of the analytical approximation and the *Gedanken* experiment is calculated by the derivative of Eq. 4 and Eq. 19 respectively. We also plot in the inset the 5% deviation from the T^3 phase accumulation, this time by plotting the derivative of the modified *Gedanken* experiment phase accumulation.

$$\Delta\phi(2T) = \left(\frac{mg^2}{24\hbar} \right)^{\frac{3+\alpha}{3}} (2T)^{3+\alpha} \rightarrow \frac{\partial\phi}{\partial(2T)} = (3+\alpha) \frac{mg^2}{24\hbar}^{\frac{3+\alpha}{3}} (2T)^{2+\alpha}, \quad (25)$$

where the exponent of the coefficient is corrected to maintain the correct units. Fig. 3(B) shows the residuals between the experimental data and the numerical simulation. To estimate the statistical noise of the phase, we use a method of error propagation from the standard deviation (STD) of the population data to the STD of the phase, which is explained in the next section.

3. Error analysis

We wish to find the phase uncertainty due to the uncertainty of a cosine signal $S(\phi) = a \cos(\phi)$, where the amplitude a and the phase ϕ have an uncertainty δa and $\delta\phi$, respectively. The uncertainty of the signal due to the phase and amplitude uncertainties is given by

$$\delta S^2 = \delta a^2 \cos^2 \phi + a^2 \sin^2 \phi \delta\phi^2. \quad (26)$$

This is a familiar relation, but it is important to remember that the trigonometric functions on the right-hand side should be averaged over the uncertainty $\delta\phi$ of the phase (otherwise this equation is not correct and gives wrong values, especially around the extremum points of the signal, where the derivative approaches zero). Assuming that ϕ is a Gaussian distributed variable with a standard deviation $\delta\phi$, the expectation values of the trigonometric functions are

$$\langle \sin^2 \phi \rangle = \frac{1}{2}[1 - \langle \cos(2\phi) \rangle], \quad \langle \cos^2 \phi \rangle = \frac{1}{2}[1 + \langle \cos(2\phi) \rangle]. \quad (27)$$

where

$$\langle \cos(2\phi) \rangle_{\phi=\phi_0} = \frac{1}{\sqrt{2\pi}\delta\phi} \int_{-\infty}^{\infty} d\phi e^{-(\phi-\phi_0)^2/2\delta\phi^2} \cos(2\phi) = \cos(2\phi_0) e^{-2\delta\phi^2} \quad (28)$$

We obtain

$$\delta S^2 = \frac{1}{2} \left[1 + \cos(2\phi) e^{-2\delta\phi^2} \right] \delta a^2 + \frac{1}{2} a^2 \left[1 - \cos(2\phi) e^{-2\delta\phi^2} \right] \delta\phi^2. \quad (29)$$

To extract the STD of the phase, we need to know the STD of the signal (δS^2), the amplitude and phase of the signal (a and ϕ), which we get from the fit to the data, and the STD of the amplitude (δa). If we want to find both amplitude and phase uncertainties from the signal uncertainties for a single point this seems to be impossible because at the right-hand-side we have two variables. So we must either assume a given value of δa and then find $\delta\phi$ from the signal uncertainty or we should assume some relation of δa and $\delta\phi$ along the different measurement points that may enable determination of both uncertainties from the signal. In our case, we assume that the amplitude uncertainty is negligible compared to the phase uncertainty, so we can find the phase uncertainty from the signal uncertainty. This assumption holds well for $2T > 1\text{ms}$, where the phase noise is the dominant source of noise in the signal, and is approximately proportional to the phase itself. While for $2T < 1\text{ms}$ this assumption is less accurate, the STD of the signal is very small in this range anyway. As the number of iterations per point is 2-4, resulting in large fluctuations of the STD, we fit the STD to a polynomial of order 3, and use the result of the fit as the STD of the phase in Fig. 3(B). The results of the error analysis are shown in Fig. 10.

J. Magnetic gradient pulses

The pulses of the magnetic gradient are formed by running a current through three parallel wires, with alternating current orientation, forming a magnetic quadrupole capable of producing high magnetic gradients with low magnetic fields. The wires are 2\mu m thick, 40\mu m wide, and are positioned 100\mu m apart (center to center), creating a quadrupole 97\mu m below the surface of the chip (see Fig. 6). The currents are produced by a homemade current source, with high stability and fast response, controlled by an analog signal input. The current source has a maximum slew rate of $30\text{mA}/\mu\text{s}$, a maximum current of 1A and stability of 100ppm . We control the current source by an arbitrary waveform generator, which allows us to create smooth and accurate pulses. To obtain a smooth pulse, we demand $I(0) = 0$, $\frac{\partial I}{\partial t}(0, \tau) = 0$, where τ is the pulse rise time. We choose to use a cosine pulse shape, as it fulfills the conditions of a smooth pulse and is analytically solvable when calculating trajectories and phases. The equation describing the current for a pulse starting at t_0 , rise and fall times of τ , separated by a duration w of constant current A is given by

$$\mathbf{I}(\mathbf{t}) : \begin{cases} 0 & \text{for } t < t_0 \\ \frac{I_{\max}}{2} \left(1 - \cos \left(\frac{\pi(t-t_0)}{\tau} \right) \right) & \text{for } t_0 < t \leq t_0 + \tau \\ I_{\max} & \text{for } t_0 + \tau < t \leq t_0 + \tau + w \\ \frac{I_{\max}}{2} \left(1 - \cos \left(\frac{\pi(t-t_0-w)}{\tau} \right) \right) & \text{for } t_0 + \tau + w < t < t_0 + 2\tau + w \\ 0 & \text{for } t \geq t_0 + 2\tau + w \end{cases} \quad (30)$$

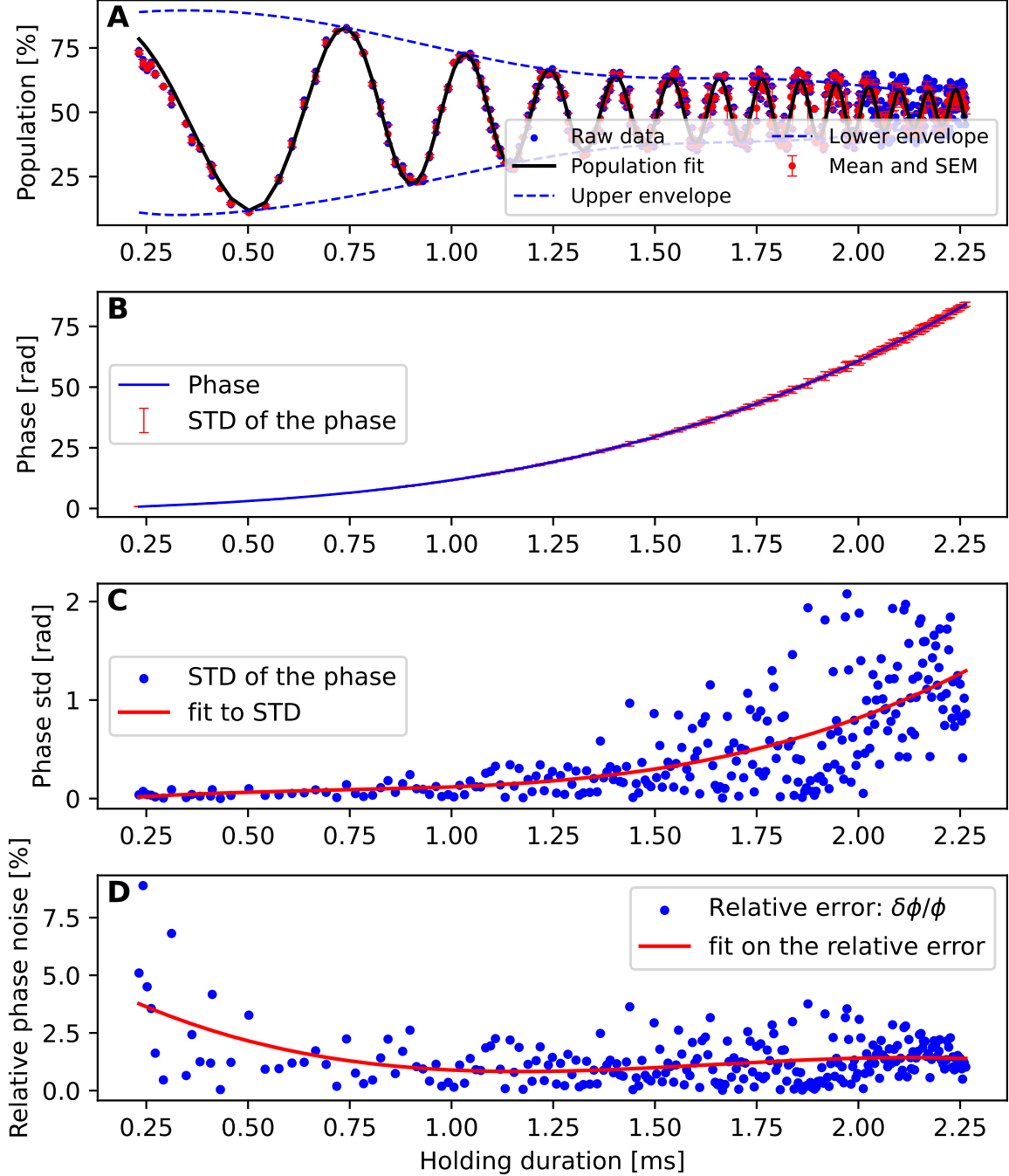


FIG. 10: Summary of the error analysis. (A) The experimental data, including the raw data of the population vs. time, the fit to the envelope, and the fit to the data. (B) The phase as a function of the holding duration, with error bars indicating the STD of the phase. The STD is calculated using the method of error propagation explained in Sec. I3. (C) The STD of the phase, and fit to a third order polynomial. The result of the fit is used as the STD of the phase in Fig. 3B (D) The relative error of the phase, calculated as the ratio of the STD of the phase to the phase, which has an average value of 1.3%.

The area under such a pulse is $I_{\max}(\tau+w)$. The scheme has two short kick pulses, and one longer holding pulse. The kick pulses have a rise and fall time of $\tau_{\text{kick}} = 40 \mu\text{s}$ each, with $w = 0$ and $I_{\max} = I_{\text{kick}}$, so that the area of the pulse is $I_{\text{kick}} \cdot \tau_{\text{kick}}$. The longer holding pulse has a rise and fall time of $\tau_{\text{hold}} = 12 \mu\text{s}$,

and a duration $w = T_h - \tau_{\text{hold}}$ of constant current I_{hold} so that the total area of the pulse is $I_{\text{hold}} \cdot T_h$.

The acceleration during the holding pulse is tuned to hold the $|1\rangle$ state against gravity. Measurement of the acceleration of the atoms shows that the required current is $I_{\text{hold}} = 23.07 \pm 1.49$ mA. To maintain the symmetry of the scheme, the momentum given by the two kick pulses should be equal to the momentum given by the holding pulse, which gives the condition

$$a_{\text{kick}} = \frac{g}{2\tau_{\text{kick}}} T_h \quad (31)$$

$$a_{\text{hold}} = g \quad (32)$$

To improve the response of the current source and reduce the effect of the ambient gradient in the chamber, we set the current between the pulses to a finite value, which we call the idle current, and set its value to $I_{\text{idle}} = 0.47$ mA. The idle is on during the entire interferometer sequence. Including the idle current, we get the following requirements for the currents

$$(I_{\text{kick}} - I_{\text{idle}}) 2\tau_{\text{kick}} = (I_{\text{hold}} - I_{\text{idle}}) T_h \quad (33)$$

$$I_{\text{kick}} = \frac{I_{\text{hold}} - I_{\text{idle}}}{2\tau_{\text{kick}}} T_h + I_{\text{idle}} \quad (34)$$

K. Magnetic potential energy of the atoms

The potential in the SGI is the magnetic potential and gravity. The magnetic potential is given by

$$V_B(\mathbf{r}, t) = -\mu \cdot B(\mathbf{r}, t).$$

Under the adiabatic approximation, we can assume that the atomic spin projection on the quantization axis, defined by the direction of the magnetic field, is conserved, and adding the second order Zeeman splitting, we get

$$V_B(\mathbf{r}, t) = m_F g_F \mu_B |B(\mathbf{r}, t)| + \alpha_{F, m_F} |B(\mathbf{r}, t)|^2 \quad (35)$$

where $g_F \mu_B / h = 0.70$ [MHz/G] and α_{F, m_F} is a coefficient that depends on F and m_F , given in table II. Using Eq. 35, the values in table II and the measured transition frequency between $|F = 2, m_F = 2\rangle$ and $|F = 2, m_F = 1\rangle$ of 8.799 MHz we can calculate the magnitude of the bias field $|B| = 12.62$ G. To calculate a_{SOZ} , we find the magnetic gradient required to hold the $|F = 2, m_F = 1\rangle$ state against gravity, and use it to get the value of $a_{SOZ} = 0.10$ m/s².

$F \backslash m_F$	0	± 1	± 2
1	-287.6	-215.7	—
2	287.6	215.7	0

TABLE II: Values of $\alpha_{F, m_F} / h$ in units of Hz/G², for calculating the second order Zeeman energy in Eq. 35.

L. Ambient gradient in the chamber

We found a small ambient magnetic gradient in the chamber even when the currents on the atom chip were zero. We measured this ambient magnetic gradient in two methods. The first method is measuring the differential acceleration between the $|1\rangle$ and $|0\rangle$ states in a long time of flight of 20 – 34 ms, after the $\pi/2$ pulse and observing the spatial splitting of the states. We fit the spatial splitting vs time and find

$a_{ambient} = 0.211 \pm 0.005 \text{ m/s}^2$. The data and the fit appear in Fig. 11. The second method is observing a T^3 phase accumulation when measuring the pure MW DD scheme for a duration of $4\tau_{DD} = 4 \text{ ms}$, which can, in the presence of the ambient gradient, create a “self emerging” T^3 full-loop SGI. In the original T^3 SGI scheme of [37], the loop is closed by inverting the orientation of the magnetic gradients. In this scheme, the magnetic gradients remain constant, and the π pulses invert the spin of the arms to create a closed interferometer. We calculate the prediction for the phase by plugging the durations $(\tau_{DD}, 2\tau_{DD}, \tau_{DD})$ and accelerations $a_1 = (a_{ambient}, 0, a_{ambient}) + g$, $a_2 = (0, a_{ambient}, 0) + g$ of the scheme into Eq. 12 which gives:

$$\delta\phi = \frac{m}{\hbar} \tau_{DD}^3 (a_{ambient}^2 + 2ga_{ambient}) , \quad (36)$$

where $\tau_{DD} = (T_h + 2T_d)/2$. Using the prediction for the phase we extract $a_{ambient} = 0.221 \pm 0.005 \text{ m/s}^2$, which corresponds to a magnetic gradient of $0.68 \pm 0.02 \text{ G/cm}$. The data and the fit of this measurement appear in Fig. 12

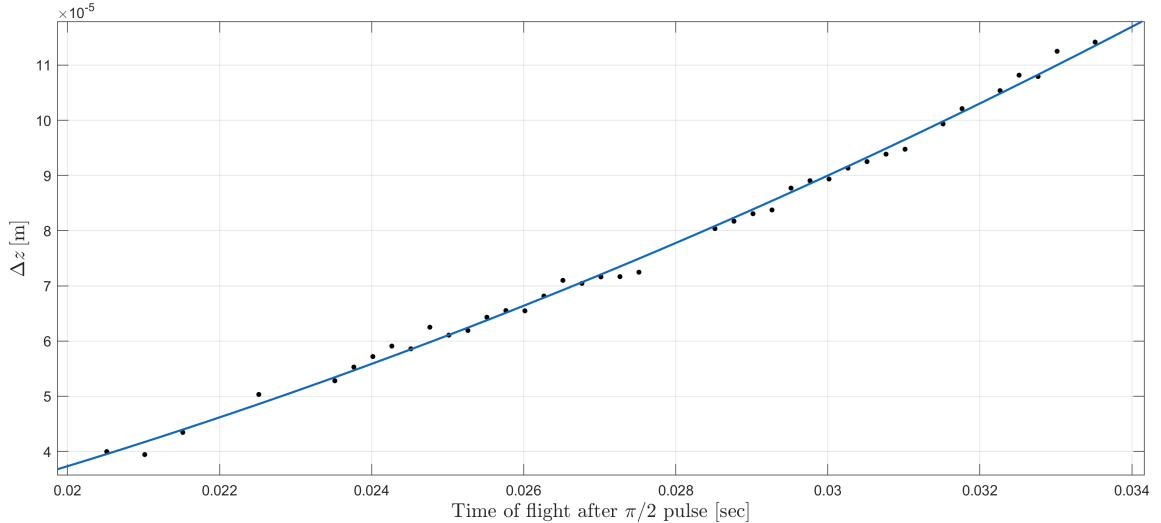


FIG. 11: Spatial SG splitting between the state $|1\rangle$ and $|0\rangle$ due to the ambient gradient, vs the time of flight after the $\pi/2$ pulse. Fitting the data to $0.5a_{ambient}TOF^2$ gives a value of $a_{ambient} = 0.211 \pm 0.005 \text{ m/s}^2$

M. Wave-packet size

Direct experimental measurement of the wave-packet size is a hard task. To begin with, our optical resolution is only $3 \mu\text{m}$. Second, imaging near the chip distorts the image due to diffraction from the chip. Diffraction also originates from the high optical density of the atom cloud. Finally, the magnetic potential of the DKC, as well as the magnetic fields during the SG kicks, are curved as they emanate from the nearby chip wires. These curvatures create lensing (focusing) effects which result in fast changes of the wave-packet size over time. Given these restrictions, when imaging the wave-packet width we observe a width of $3 - 4 \mu\text{m}$ on the CCD, which indicates that the actual size is most probably below our optical resolution.

A better estimation of wave-packet size is derived using our accurate numerical simulation (Fig. 13). The simulation shows that at half way through the interferometer, the wave-packet size is in the range of $1 - 1.3 \mu\text{m}$. The maximum splitting achieved is thus 6.5 times the wave-packet width.

Achieving a larger splitting is feasible but would require significant changes in the experiment, even if we assume that environmental decoherence will not increase for the larger splitting and for the longer duration which is associated with it. The main reason that achieving larger splitting is hard is due to a diminishing overlap and contrast emanating from differential changes of wave-packet size and shape

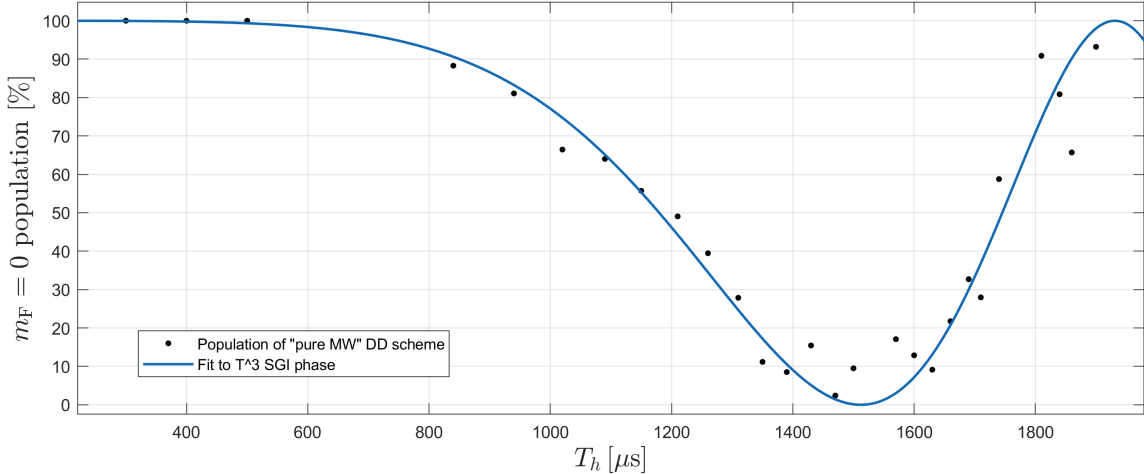


FIG. 12: T^3 population oscillations in a pure MW DD scheme. By fitting the data to $P(\tau_{DD}) = 50 + 50 \cos \left[\frac{m}{\hbar} \tau_{DD}^3 (a_{ambient}^2 + 2ga_{ambient}) \right]$, we can estimate the acceleration due to the ambient gradient, and get $a_{ambient} = 0.221 \pm 0.005 \text{ m/s}^2$.

formed by the magnetic potential curvatures discussed above. The larger the required magnetic kicks are, the stronger these effects become. Hence, one would have to create larger gradients (for larger splitting) while suppressing the field curvature. While the curvature goes like I/r^3 (r is the distance to the chip and I is the current), the gradient goes like I/r^2 , so in order to increase the gradient by 2(10) while suppressing the curvature by 2(10), the distance to the chip would have to be increased by a factor of 4(10^2) and the current would have to increase by a factor of 32(10^5). For various technological barriers, even the smaller numbers pose a significant challenge.

N. Connection between gauge phase and equivalence principle

This theoretical summary establishes the connection used in the introduction of the paper between the gauge phase and the equivalence principle. We follow the presentation given in [3, 29] as well as [20]. We will assume, as noted in the introduction, that the inertial mass and gravitational mass are identical. The Lagrangian for a particle with mass m moving in an accelerated frame with the acceleration given by g (Einsteinian frame) is:

$$L_E = \frac{1}{2}m(\dot{z} + gt)^2, \quad (37)$$

whereas for a particle moving in the gravitational potential mgz , the Lagrangian (Newtonian frame) is

$$L_N = \frac{1}{2}m(\dot{z})^2 - mgz = L_E + \frac{d}{dt}\Lambda(z, t) \quad (38)$$

where

$$\Lambda = -mgzt - \frac{1}{6}mg^2t^3 \quad (39)$$

can be regarded as a gauge transformation. The quantum state in the freely falling coordinate system, Ψ_E , and the quantum state in the inertial (laboratory) coordinate system, Ψ_N , as expressed in the position basis, are related as follows [3, 29]:

$$\Psi_N = e^{\frac{i}{\hbar}\Lambda(z, t)}\Psi_E. \quad (40)$$

This relation holds for all the solutions of the corresponding Schrödinger equations, one, where the particle is freely falling; the other, where the particle is in a uniform gravitational field [3]. In the

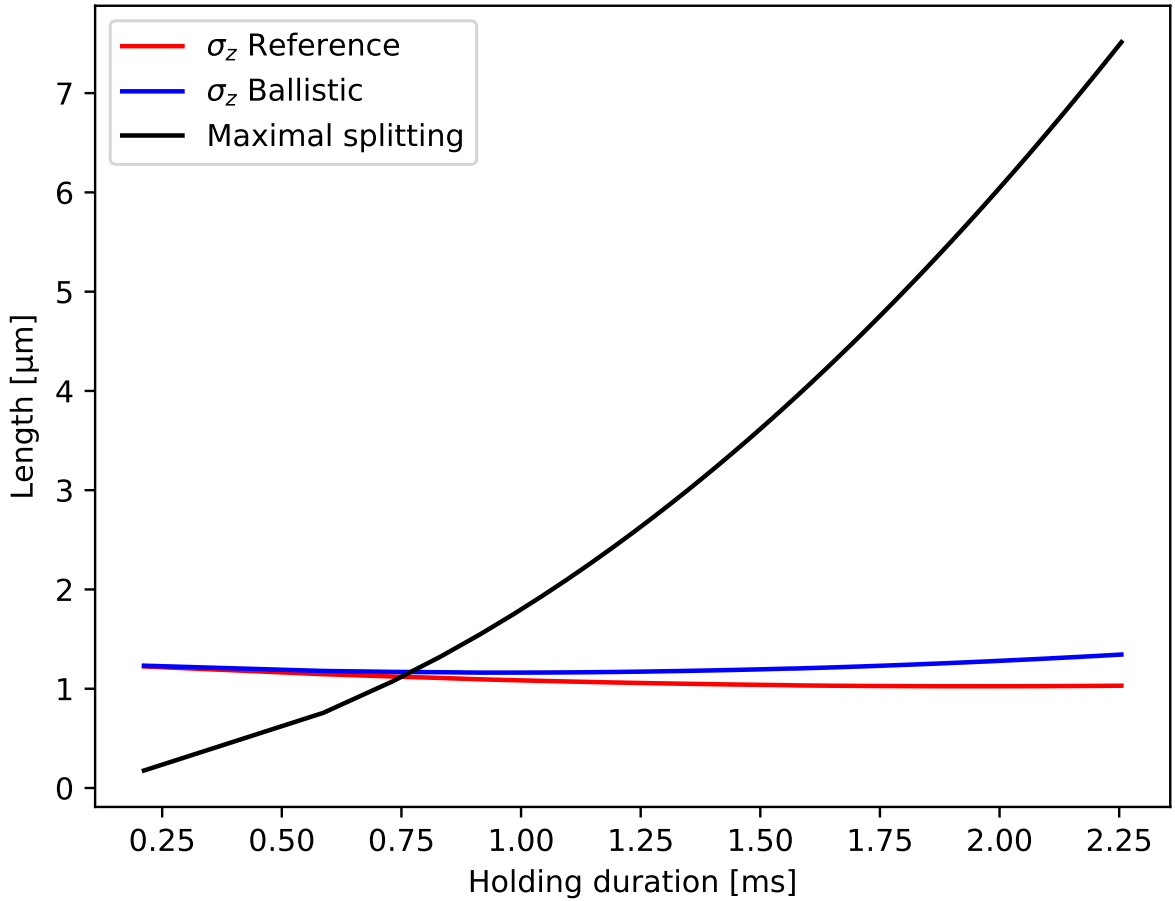


FIG. 13: Numerical calculation of the wave-packet size and the maximal splitting for different interferometer durations. The wave-packet width is defined by the Gaussian width of the wave packet along the z axis. At the largest holding duration the maximal splitting is $7.5 \mu\text{m}$, and the wave-packet widths are $1 \mu\text{m}$ and $1.3 \mu\text{m}$, for the reference and ballistic wave packets respectively.

classical domain a gauge symmetry means that two distinct Lagrangians lead to identical equations of motion — hence the difference between the Lagrangians is unobservable. In this sense the equivalence principle (EP) can be regarded as a gauge symmetry, because, classically, the two Lagrangians of Eq. (37) and (38) lead to the same dynamical evolution. In the quantum domain, the gauge symmetry means that these two distinct Lagrangians lead to quantum evolutions that differ only by the phase [Eq. (39)], point by point. The fact that this phase is an overall phase factor multiplying the wavefunction makes it empirically inaccessible at any one point: this ensures that quantum theory satisfies the EP as a gauge principle — locally, as there is no way of detecting the difference between the two dynamics generated, respectively, by Eqs. (37) and (38). However, in quantum theory, this overall phase can always lead to detectable phase difference by having a superposition across different points, so that the wavefunction at each point develops a different phase — producing an observable phase difference. The QGI implements such a superposition and it is the measurement of this relative phase that is observable. Of course, one can always redefine (by a coordinate change) the phase locally, at one point; however, a corresponding change has then to occur at other points so that the relative phase remains invariant, as the gauge principle requires.

O. Einstein equivalence principle for Maxwell waves

The identity of inertial and gravitational mass, usually referred to as the *weak* equivalence principle [1], led Albert Einstein to a generalized equivalence principle: locally a constant gravitational field is indistinguishable from a constant acceleration.

However, the impossibility of distinguishing between a frame with gravity and the one that is accelerated imposes that the laws of physics must be identical in these two systems. This form of the equivalence principle is usually referred to as the *Einstein* equivalence principle [2]. Here we neglect the gravitational field of the test mass. When we include the gravitational interaction, for example, for a stellar object, it is called the *strong* equivalence principle.

In this section we compare and contrast the Kasevich-Chu interferometer (KCI) and the QGI. This analysis brings out most clearly that it is the difference in the beam splitters which leads in the KCI to a confirmation of the Einstein equivalence principle of Maxwell waves [42], whereas in QGI it is a confirmation of the Einstein equivalence principle for de-Broglie waves.

In KCI the beam splitters and mirrors are formed [42] by an optical two-photon transition in a Λ -system which is detuned with respect to the upper level. Although the frequency difference of the transition between the ground state and the third level is in the microwave regime, the total momentum transfer determined by the wave vector k of the light fields reads $2\hbar k$, since the light fields are counter propagating. We emphasize that in the KCI, the momentum transfer is always $2\hbar k$ independent of the momentum of the scattered atom.

In contrast, in the QGI the beam splitters and the mirrors are realized by two different mechanisms. Indeed, the linear gravitational potential and the magnetic field gradient during the ballistic motion (holding time) act as mirrors where every momentum is, in principle, perfectly inverted. It is this feature which ensures the symmetry between the reference and the ballistic wave packet, as shown in Table I. The beam splitters in the QGI ($\pi/2$ MW pulses) create the coherent superposition between two internal states of the atom without transferring a substantial momentum. It is the magnetic-gradient pulses which launch and stop the ballistic wave packet.

Next we compare and contrast the KCI in the Newtonian and the Einsteinian frame. In the Newtonian frame, the atom in the two paths of the interferometer feels the gravitational acceleration and the phase difference is proportional to the square of the time the atom spends in the interferometer, and linear in acceleration. Since there is no difference in the accelerations in the two paths, the cubic phase in the two paths cancels out. In this description the phase of the electromagnetic fields is constant.

In the Einsteinian frame attached to the atom there is no gravity. However, the frequency of the electromagnetic wave is linearly chirped due to the acceleration of the atom. In this frame the phase shift obviously does not arise from gravity but from the chirping of the laser pulses with the rate given by the gravitational acceleration.

It is important to note that experiments [60] determining the gravitational acceleration in the Newtonian frame vary the chirp rate a and record the phase difference in the KCI as a function of a . Since the phase difference is linear in the effective acceleration, it is now given by the difference of the chirp rate and the gravitational acceleration. Hence, when the rate is equal to the gravitational acceleration the phase shift vanishes and is thus independent of the interferometer time.

This technique would not work if the electromagnetic wave would not transform accordingly. Hence, this measurement technique based on the KCI is a manifestation of the Einstein equivalence principle for Maxwell waves.

We conclude by comparing and contrasting this aspect to the QGI. In the KCI, the interaction with the atoms is very sensitive to a resonance condition, due to a significant Doppler shift $\mathbf{k} \cdot \mathbf{v}$. Therefore, changing reference frames, which amounts to changing the velocity of the atoms, must be accompanied by an adequate change of the electromagnetic field frequency, and the transformation of the electromagnetic fields of the beam splitters and mirrors plays an important role in the KCI. In contrast, in the QGI, the magnetic-gradient pulses - the Fourier-Transform of which may be considered as an electromagnetic wave having a frequency of about 10 kHz - do not require a resonance condition to interact efficiently with the atoms. Furthermore, the Rabi frequency of the MW pulses responsible for the internal spin splitting and spin inversion is much larger than the Doppler shift. Hence, no transformation of MW fields between the two frames is required in the QGI interferometer.

P. Future experiments with nano-particles

It should be pointed out that the considerations of this paper refer to the gravitational field as a “passive” background, namely the Earth’s gravitational field, which is not being actively affected by the quantum-mechanical constituents of the atom in the experiment itself. Such influences would be far too tiny to have any effect on the behaviour of the system under consideration.

The distinction between active and passive mass [61] goes back to Newton, when he compared the Earth’s active mass on the falling apple with the Earth’s passive mass in its motion around the Sun, in its response to the Sun’s active mass.

The Díosi-Penrose proposal for the life-time for quantum state-reduction arises from the active effect of bodies in quantum superposition and represents a vital area of future experimentation. It is argued that when mass plays an active role in the quantum superpositions then the quantum evolution becomes problematic, suggesting a time-scale for quantum state reduction. This could be regarded as a conflict with the equivalence principle as formulated by Marletto and Vedral [20]. In fact, the equivalence principle, as normally considered refers only to the passive effects of mass.

In order to probe the issue of whether active gravitational effects do actually induce the decay of superpositions, one must achieve quantum coherences persisting for at least a second, with mass scales on the order of 10^9 to 10^{10} atomic masses. Presently, the most massive superpositions reached in the laboratory—those involving large molecules—remain at least six to seven orders of magnitude below this threshold [62]. Ongoing experimental efforts, employing nanoparticles, micromechanical mirrors, and nanodiamonds, aim to bridge this gap and reach the necessary regime.

[1] Focus issue: Tests of the weak equivalence principle, Eds. C. C. Speake and C. M. Will, *Classical and Quantum Gravity* **29** (2012).

[2] C. M. Will, The Confrontation between General Relativity and Experiment, *Living Rev. Relativ.* **17**, 4 (2014).

[3] M. Nauenberg, Einstein's equivalence principle in quantum mechanics revisited, *American Journal of Physics* **84**, 879 (2016).

[4] R. Colella, A. W. Overhauser, and S. A. Werner, Observation of Gravitationally Induced Quantum Interference, *Phys. Rev. Lett.* **34**, 1472 (1975).

[5] U. Bonse & T. Wroblewski, Measurement of Neutron Quantum Interference in Noninertial Frames, *Phys. Rev. Lett.* **51**, 1401 (1983).

[6] A. Peters, K. Y. Chung, and S. Chu, High-precision gravity measurements using atom interferometry, *Metrologia* **38**, 25 (2001).

[7] J. B. Fixler, G. T. Foster, J. M. McGuirk, and M. A. Kasevich, Atom Interferometer Measurement of the Newtonian Constant of Gravity, *Science* **315**, 74 (2007).

[8] G. Rosi et al., Quantum test of the equivalence principle for atoms in coherent superposition of internal energy states, *Nat. Commun.* **8**, 15529 (2017).

[9] G. M. Tino, Testing gravity with cold atom interferometry: results and prospects, *Quantum Science and Technology* **6**, 024014 (2021).

[10] C. D. Panda et al., Measuring gravitational attraction with a lattice atom interferometer, *Nature* **631**, 515 (2024).

[11] E. Okon & C. Callender, Does quantum mechanics clash with the equivalence principle—and does it matter?, *Euro. J. Phil. Sci.* **1**, 133 (2011).

[12] C. Lämmerzahl, On the Equivalence Principle in Quantum Theory, *General Relativity and Gravitation* **8**, 1043 (1996).

[13] H. C. Rosu, Classical and quantum inertia: a matter of principle, *Gravit. Cosmol.* **5**, 81 (1999).

[14] H. Padmanabhan & T. Padmanabhan, Nonrelativistic limit of quantum field theory in inertial and noninertial frames and the principle of equivalence, *Phys. Rev. D* **84**, 085018 (2011).

[15] S. T. Pereira & R. M. Angelo, Galilei covariance and Einstein's equivalence principle in quantum reference frames, *Phys. Rev. A* **91**, 022107 (2015).

[16] M. Zych & Č. Brukner, Quantum formulation of the Einstein equivalence principle, *Nature Phys.* **14**, 1027 (2018).

[17] F. Giacomini, E. Castro-Ruiz & Č. Brukner, Quantum mechanics and the covariance of physical laws in quantum reference frames, *Nature Comm.* **10**, 494 (2019).

[18] L. Hardy, arXiv:1903.01289, (2019).

[19] S. Das, M. Fridman & G. Lambiase, General formalism of the quantum equivalence principle, *Comm. Phys.* **6**, 198 (2023).

[20] C. Marletto & V. Vedral, On the Testability of the Equivalence Principle as a Gauge Principle Detecting the Gravitational T^3 Phase, *Front. Phys.* **8**, 176 (2020).

[21] R. Howl, R. Penrose & I. Fuentes, Exploring the unification of quantum theory and general relativity with a Bose–Einstein condensate, *New Journal of Physics* **21**, 043047 (2019).

[22] T. A. Wagner, S. Schlamming, J. H. Gundlach, & E. G. Adelberger, Torsion-balance tests of the weak equivalence principle, *Classical Quantum Gravity* **29**, 184002 (2012).

[23] P. Touboul et al., MICROSCOPE Mission: First Results of a Space Test of the Equivalence Principle, *Phys. Rev. Lett.* **119**, 231101 (2017).

[24] P. Asenbaum, C. Overstreet, M. Kim , J. Curti, & M. A. Kasevich, Atom-Interferometric Test of the Equivalence Principle at the 10^{-12} Level, *Phys. Rev. Lett.* **125**, 191101 (2020).

[25] As an interesting contextual anecdote, one may say that the mathematical description of free fall, as discovered by Galileo, is governed by powers of t : the acceleration is proportional to t^0 , the velocity to t^1 , and the position to t^2 . In this work we extend this framework and demonstrate experimentally that the quantum phase of a freely falling mass follows a t^3 power law.

[26] C. G. Darwin, Free motion in the wave mechanics, *Proc. R. Soc. Lond. A* **117**, 258 (1927).

[27] E.H. Kennard, Zur Quantenmechanik einfacher Bewegungstypen, *Zeitschrift für Physik* **44**, 326 (1927).

[28] E.H. Kennard, The quantum mechanics of an electron or other particle, *Journal of the Franklin Institute* **207**, 47 (1929).

[29] D. M. Greenberger & A. W. Overhauser, Coherence effects in neutron diffraction and gravity experiments, *Rev. Mod. Phys.* **51**, 43 (1979).

[30] H. Beyer & J. Nitsch, The non-relativistic cow experiment in the uniformly accelerated reference frame, *Phys. Lett. B* **182**, 211 (1986).

[31] R. Penrose, *The Road to Reality*, Vintage (2007).

[32] R. Penrose, Black holes, quantum theory and cosmology, *Journal of Physics: Conference series* **174**, 012001 (2009).

[33] R. Penrose, On the Gravitization of Quantum Mechanics 1: Quantum State Reduction, *Foundations of Physics* **44**, 557 (2014).

[34] M. Zimmermann et al., T^3 -Interferometer for atoms, *Appl. Phys. B* **123**, 102 (2017).

[35] G. D. McDonald et al., A faster scaling in acceleration-sensitive atom interferometers, *Europhys. Lett.* **105**, 63001 (2014).

[36] I. Dutta, D. Savoie, B. Fang, B. Venon, C.L. Garrido Alzar, R. Geiger, and A. Landragin, Continuous Cold-Atom Inertial Sensor with 1 nrad/sec Rotation Stability, *Phys. Rev. Lett.* **116**, 183003 (2016).

[37] O. Amit, Y. Margalit, O. Dobkowski, Z. Zhou, Y. Japha, M. Zimmermann, M. A. Efremov, F. A. Narducci, E. M. Rasel, W. P. Schleich, & R. Folman, T^3 Stern-Gerlach Matter-Wave Interferometer, *Phys. Rev. Lett.* **123**, 083601 (2019).

[38] G. G. Rozenman et al., Amplitude and Phase of Wave Packets in a Linear Potential, *Phys. Rev. Lett.* **122**, 124302 (2019).

[39] E. Zuniga, E. Gomez and L. O. Castanos-Cervantes, Limits of magnetic T^3 -atomic gravimetry due to atomic cloud expansion, *Phys. Rev. A* **109**, 013304 (2024).

[40] Let us note that the ballistic frame [as defined by Fig. 1(A)] and the standard freely-falling frame (monotonically increasing velocity towards Earth) are the same up to the constant velocity v_0 . As physics is invariant to such a constant velocity shift, our ballistic frame may be regarded as a freely-falling frame.

[41] Let us note that if one computes the relative phase from both frames, and does so in the same order, the phase difference comes out with a different sign depending on from which frame you made the calculation. This sign has no observable effect in our setup as the observable interference fringes are the result of a cosine function which is not sensitive to the sign.

[42] W. Schleich et al., A representation-free description of the Kasevich–Chu interferometer: a resolution of the redshift controversy, *New. J. Phys.* **15**, 013007 (2013).

[43] E. Giese et al., Proper time in atom interferometers: Diffractive versus specular mirrors, *Phys. Rev. A* **99**, 013627 (2019).

[44] T. Kovachy et al., Quantum superposition at the half-metre scale, *Nature* **528**, 530 (2015).

[45] V. Xu et al., Probing gravity by holding atoms for 20 seconds, *Science* **366**, 745 (2019).

[46] K. A. Krzyzanowska, Matter-wave analog of a fiber-optic gyroscope, *Phys. Rev. A* **108**, 043305 (2023).

[47] M. Keil et al., Fifteen years of cold matter on the atom chip: Promise, realizations and prospects, *J. Modern Optics* **63**, 1840 (2016).

[48] M. Keil et al., Stern-Gerlach interferometry with the atom chip, Book in honor of Otto Stern, In: B. Friedrich, H. Schmidt-Böcking (eds.) *Molecular Beams in Physics and Chemistry*. Springer, Cham. (2021).

[49] Y. Margalit et al., Realization of a complete Stern-Gerlach interferometer: Toward a test of quantum gravity, *Sci. Adv.* **7**, 2879 (2021).

[50] Y. Japha & R. Folman, Quantum uncertainty limit for Stern-Gerlach interferometry with massive objects, *Phys. Rev. Lett.* **130**, 113602 (2023).

[51] J.N. Kirsten-Siemss et al., Large-momentum-transfer atom interferometers with μ rad-accuracy using Bragg diffraction, *Phys. Rev. Lett.* **131**, 033602 (2023).

[52] Y. Japha, Unified model of matter-wave-packet evolution and application to spatial coherence of atom interferometers, *Phys. Rev. A* **104**, 053310 (2021).

[53] C. Bordé, Atomic interferometry with internal state labelling, *Phys. Lett. A* **140**, 10 (1989).

[54] M. Kasevich and S. Chu, Atomic Interferometry Using Stimulated Raman Transitions, *Phys. Rev. Lett.* **67**, 181 (1991).

[55] Y. Margalit et al., A self-interfering clock as a “which path” witness, *Science* **349**, 1205 (2015).

[56] F. Di Pumbo, A. Friedrich, C. Ufrecht & E. Giese, Universality-of-clock-rates test using atom interferometry with T^3 scaling, *Phys. Rev. D* **107**, 064007 (2023).

[57] J.M. Lévy-Leblond, Nonrelativistic particles and wave equations. *Commun. Math. Phys.* **6**, 286 (1967).

[58] K. A. Whittaker, J. Keaveney, I. G. Hughes & C. S. Adams, Hilbert transform: Applications to atomic spectra, *Physical Review A* **91**, 032513 (2015).

[59] G. G. Rozenman et al., Projectile motion of surface gravity water wave packets: An analogy to quantum mechanics, *The European Physical Journal Special Topics* **230**, 931 (2021).

[60] D. Schlippert et al., Quantum Test of the Universality of Free Fall, *Phys. Rev. Lett.* **112**, 203002 (2014).

[61] H. Bondi, Negative Mass in General Relativity, *Rev. Mod. Phys.* **29**, 423 (1957).

[62] S. Bose et al., Massive quantum systems as interfaces of quantum mechanics and gravity, *Rev. Mod. Phys.* **97**, 015003 (2025).